

# Effect of Alloying Elements in Hot-Rolled Metastable $\beta$ -Titanium Alloys: Part I. Evolution of Microstructure and Texture

PREMKUMAR MANDA, P. GHOSAL, UDAY CHAKKINGAL, and A.K. SINGH

The present work describes the evolution of microstructures and textures in alloys Ti-5Al-5Mo-5V-3Cr (A1), Ti-5Al-3.5Mo-7.2V-3Cr (A2), Ti-5Al-5Mo-8.6V-1.5Cr (A3), and Ti-5Al-3.5Mo-5V-3.94Cr (A4) during unidirectional hot rolling. The hot-rolled microstructures of the alloy A1 exhibit large fraction of recovered/recrystallized grains, while the alloy A3 shows small fraction of recovered/recrystallized grains. The alloy A2 displays subgrains and recrystallized grains, while the alloy A4 exhibits the microstructure consisting of the features of both the alloys A1 and A2. The alloys A1, A3, and A4 show the presence of shear bands within the  $\beta$  grains and also small volume fraction of the  $\alpha$  phase. The dominance of deformation and/or recrystallization components in respective  $\alpha$  and  $\gamma$  fibers varies with alloy compositions and hot rolling reductions. In alloys A1 and A2, deformation components dominate from 30 to 50 pct rolling reductions, while recrystallization components govern in 70 pct rolled samples. The deformation components prevail from 30 to 70 pct rolling reductions in alloy A3. The alloy A4 exhibits softening of texture due to recovery or early stage of recrystallization from 30 to 50 pct reductions, while texture present in 70 pct rolled sample consists of mainly the deformation components. The role of molybdenum appears to be quite critical in the evolution of microstructures and textures of these alloys. The alloys with low and high Mo contents display high and low amount of the  $\alpha$  phase, respectively.

DOI: 10.1007/s11661-015-2814-7

© The Minerals, Metals & Materials Society and ASM International 2015

## I. INTRODUCTION

TITANIUM and its alloys are widely used in the aerospace industry due to their high strength-to-density ratio and very good mechanical properties.<sup>[1-7]</sup> These alloys can be classified as  $\alpha$ , near  $\alpha$ ,  $\alpha + \beta$ , metastable  $\beta$ , and  $\beta$  depending upon the amount of alloying elements and the volume fraction of the  $\beta$  phase. The high-temperature  $\beta$  (bcc) phase can be retained in metastable  $\beta$ -titanium alloys at room temperature by larger additions (10 to 15 wt pct) of  $\beta$  stabilizing elements.<sup>[8-10]</sup>  $\beta$ -titanium alloys belong to one of the versatile classes of materials with respect to processing, microstructures, and mechanical properties. Even though the  $\alpha + \beta$  alloy Ti-64 (Ti-6Al-4V) dominates in the aerospace industry, use of  $\beta$  or metastable  $\beta$ -titanium alloys has grown substantially during the last 10 to 15 years. Boeing 777 is the first commercial aircraft in which a large number of components, fabricated by  $\beta$  titanium alloy Ti-1023 (Ti-10V-2Fe-3Al), have been used.<sup>[11]</sup> The components of Ti-64 are replaced by the alloy Ti-1023 because of its high strength and better fatigue properties. The metastable  $\beta$ -titanium alloys such as Ti-1023, Ti-55511

(Ti-5Al-5Mo-5V-1Cr-1Fe), and Ti-5553 (Ti-5Al-5Mo-5V-3Cr) are heat-treatable titanium alloys which possess good combination of strength, fracture toughness, fatigue properties, deep hardenability, and reasonable ductility.<sup>[5,12,13]</sup> The alloy Ti-5553 has been derived from the Russian alloy VT-22 to replace Ti-1023 in some of the structural components of the aircraft. It is used to manufacture the key components of the main landing gear in Boeing-787 and Airbus-A380 aircrafts due to its high strength.<sup>[14-18]</sup>

The high strength in metastable  $\beta$ -titanium alloys is because of fine  $\alpha$  precipitates. The  $\alpha$  phase can form either by heat treatment below the  $\beta$  transus temperature or during slow cooling from the  $\beta$  phase field. The precipitation of an  $\alpha$  phase in  $\beta$ -titanium alloys takes place either heterogeneously or homogeneously. In the former case, the  $\alpha$  phase forms on the primary  $\beta$  grain boundaries as continuous layer, while in the latter case, the  $\alpha$  precipitates on both the grain boundaries as well as within the grains. These  $\alpha$  precipitates introduce large number of  $\alpha/\beta$  phase boundaries which act as dislocation barriers and thereby increases the strength. The mechanical properties obtained from these heat treatments are, therefore, a function of morphology, volume fraction, size, and distribution of the  $\alpha$  phase within the  $\beta$  matrix.<sup>[19]</sup>

These alloys are used in industrial applications with either a lamellar or bi-modal microstructure. Lamellar structures possess high fracture strength and show superior resistance to creep. These structures are a result of simple cooling from temperatures above the  $\beta$ -transus. The bi-modal microstructure is a combination of the equiaxed primary  $\alpha$  phase and the lamellar

PREMKUMAR MANDA, P. GHOSAL, and A.K. SINGH, Scientists, are with the Defence Metallurgical Research Laboratory, Hyderabad 500 058, India. Contact e-mail: singh\_ashok3@rediffmail.com UDAY CHAKKINGAL, Professor, is with the Department of Metallurgical and Materials Engineering, Indian Institute of Technology Madras (IIT Madras), Chennai 600 036, India.

Manuscript submitted October 7, 2014.

Article published online March 17, 2015

structure and can be obtained by first hot working the alloy in the  $\alpha + \beta$  phase field and then solution treatment and aging. Generally, the microstructures of metastable  $\beta$ -titanium alloys are very sensitive to thermomechanical processing. As a result, these alloys need to be processed under isothermal or near isothermal conditions at relatively low temperatures in order to control microstructure and mechanical properties.<sup>[20]</sup>

The lamellar  $\alpha$  phase cannot be fragmented to globular or equiaxed during heat treatment. Therefore, thermomechanical processing of these alloys is carried out in the  $\alpha + \beta$  phase field to obtain different volume fractions and morphologies of  $\alpha$  phase.<sup>[21,22]</sup> The corresponding structural modifications in terms of microstructure and texture resulting from thermomechanical processing, in turn, govern the mechanical properties of these alloys. The flow behavior of the alloy Ti-5553 in relation to process temperatures, strain rate, initial microstructural condition, and the influence of lubrication has been studied by Jones *et al.*<sup>[23]</sup> Investigation of microstructure and texture developed during hot rolling of the alloy Ti-5553 is rather limited. The present work is thus concerned with the evolution of microstructures and textures of Ti-5553 and the other three alloys with the same Mo equivalent in unidirectionally hot rolled in the  $\alpha + \beta$  phase field with different reductions.

## II. EXPERIMENTAL

Four experimental alloys with nominal compositions Ti-5Al-5Mo-5V-3Cr, Ti-5Al-3.5Mo-7.2V-3Cr, Ti-5Al-5Mo-8.6V-1.5Cr, and Ti-5Al-3.5Mo-5V-3.94Cr designated as A1, A2, A3, and A4, respectively, were prepared using non-consumable vacuum arc melting.

Initially, raw materials (charge) were blended and kept in a water-cooled copper crucible under a vacuum of  $10^{-3}$  mbar. The copper crucible was filled with argon gas, and then the arc was struck between the thoriated tungsten electrode and the charge. The melting begins after the stable arc is established. A total of 600 g pancake of each alloy was melted six times to ensure chemical homogeneity. The chemical composition of alloy A1 is same as the Ti-5553, while the other three alloys (A2, A3, and A4) were selected by keeping Mo equivalent constant (8.15) with different combinations of Mo, V, and Cr. The Mo equivalent is defined as the sum of the weighted averages of the elements (wt pct) present in the alloy.<sup>[20]</sup> This is given as

$$\begin{aligned} \text{Mo}_{\text{eq}} = & \text{Mo} + 0.67\text{V} + 0.44\text{W} + 0.28\text{Nb} + 0.22\text{Ta} \\ & + 1.6\text{Cr} + 1.25\text{Ni} + 1.7\text{Co} + 2.9\text{Fe} \\ & - 1.0\text{Al} \text{ (Wt pct)}. \end{aligned} \quad [1]$$

The chemical compositions of all four alloys have been determined by inductively coupled plasma-optical emission spectroscopy (ICP-OES). The interstitial elements such as C, O, N, and H were measured using inert gas fusion technique. The analyzed chemical compositions of all four alloys are given in Table I.

The beta transus temperatures ( $\beta_t$ ) of all the four alloys have been determined by differential scanning calorimetry (DSC) experiments (Setaram, Instrumentation) and theoretically calculated using Yoltan formula.<sup>[24]</sup> These values are given in Table II. The pancakes of all four alloys were initially forged up to 20 pct reduction in  $\alpha + \beta$  phase field [ $\beta_t$ -298 K (25 °C)] and then air cooled (AC). This has been used as starting material for hot rolling. The forged materials were

**Table I. Chemical Composition of the Experimental Alloys**

Alloy Designation	Nominal Composition (wt pct)					Analyzed Composition (wt pct)				Interstitial Elements (wt pct)				
	Al	Mo	V	Cr	Ti	Al	Mo	V	Cr	C	O	N	H	Ti
A1	5.0	5.0	5.0	3.0	balance	5.17	4.96	4.85	2.98	0.021	0.10	0.007	0.016	balance
A2	5.0	3.5	7.2	3.0	balance	5.10	3.30	7.30	3.20	0.075	0.04	0.017	0.012	balance
A3	5.0	5.0	8.6	1.5	balance	5.25	4.52	8.75	1.50	0.025	0.12	0.005	0.005	balance
A4	5.0	3.5	5.0	3.9	balance	5.41	3.18	5.25	4.16	0.035	0.13	0.005	0.005	balance

**Table II. Beta Transus Temperatures Obtained by DSC and Theoretical Calculation and Corresponding Hot Rolling Temperatures Used in Present Study**

S. No.	Alloy Designation	$\beta_t$ (°C) Calculated Using Yoltan Formula <sup>[24]</sup>	$\beta_t$ (°C) Determined Using DSC	Hot Rolling Temperature [ $\beta_t$ -298 K (25 °C)]
1	A1	852	850	825
2	A2	829	818	793
3	A3	830	820	795
4	A4	849	864	839

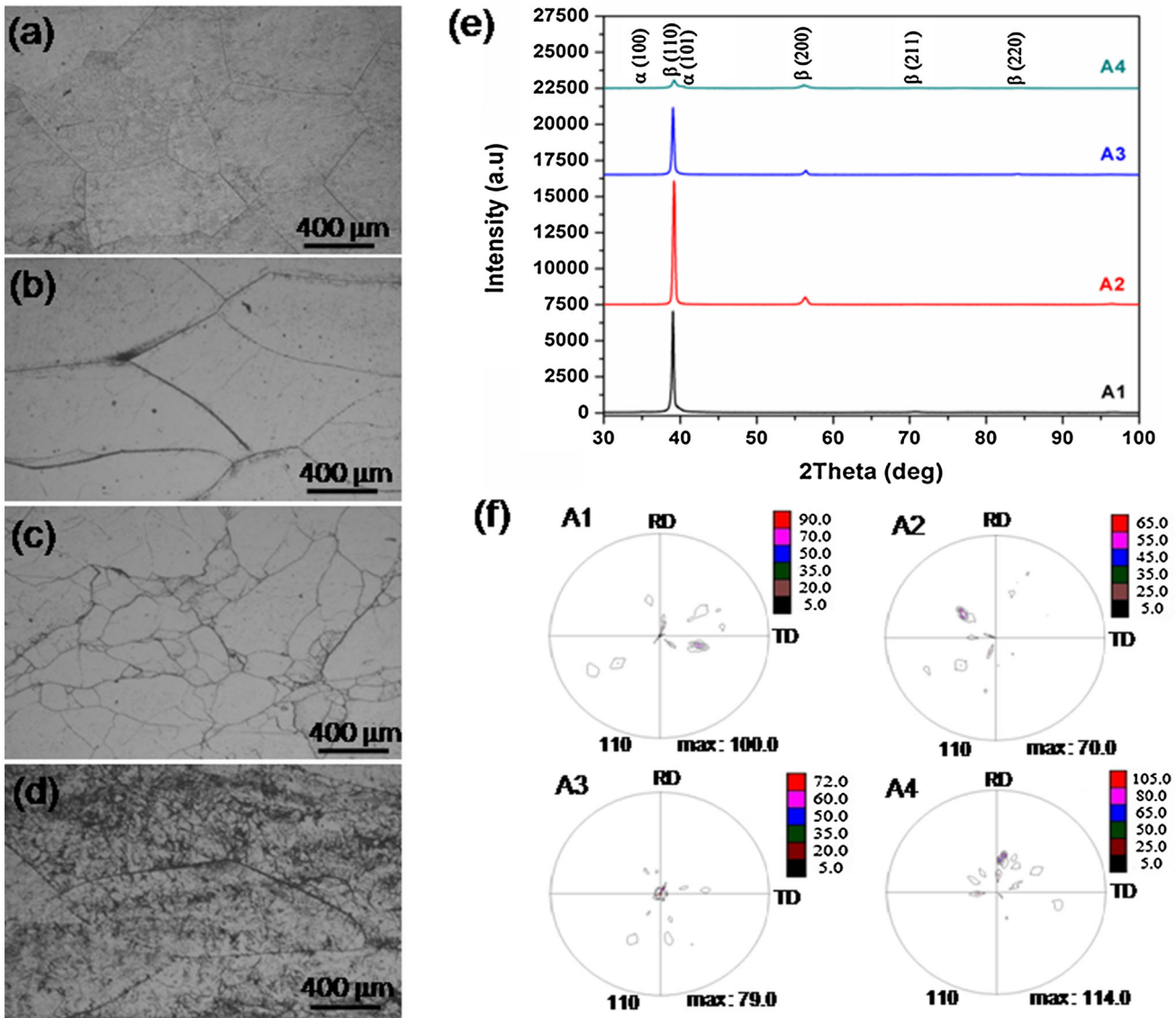


Fig. 1—Microstructures of the as-cast alloys: (a) A1, (b) A2, (c) A3, (d) A4, (e) corresponding XRD patterns, and (f) {110} pole figures.

subjected to unidirectional hot rolling in  $\alpha + \beta$  phase field with 30, 50, and 70 pct reductions and then AC. Hot rolling temperatures of all four alloys are given in Table II. A two-high rolling mill (DEMAG, Germany) has been used for hot rolling. The forged alloys were deformed by 8 pct in each pass, and rolling direction was kept strictly unidirectional. After each pass, the samples were put back into the furnace for 15 minutes in order to re-attain the rolling temperature.

The as-cast and hot-rolled samples for optical and scanning electron microscopy (OM and SEM) and texture measurements were prepared following standard metallographic techniques used for titanium and its alloys, and etched with modified Kroll's reagent [94 mL H<sub>2</sub>O, 4 mL HNO<sub>3</sub>, and 2 mL HF]. The microstructures of as-cast and rolled samples were examined using optical microscope. The microstructural characterization of the hot-rolled specimens was carried using a Leo

440i SEM in back-scattered electron (BSE) imaging mode. Electron back-scattered diffraction (EBSD) experiments were carried out with FEG-SEM, SUPRA™ 55, ZEISS make coupled with EBSD detector system NORDLYS II and with HKL channel 5 software. The XRD patterns were recorded using a Philips PW3020 diffractometer equipped with a graphite monochromator operated at 40 kV and 25 mA. Texture measurements from the mid sections of the specimens were carried out using Schultz reflection technique by INEL XRG 3000 X-ray diffractometer equipped with position sensitive detector with Cu K $\alpha$  radiation. Three experimental pole figures {110}, {200}, and {211} were used to calculate Orientation Distribution Function (ODF) plots and complete pole figures using LaboTex software. Orthorhombic sample symmetry has been employed for the ODF calculations. The ODF plots are represented as constant  $\varphi_1$  sections with iso-intensity

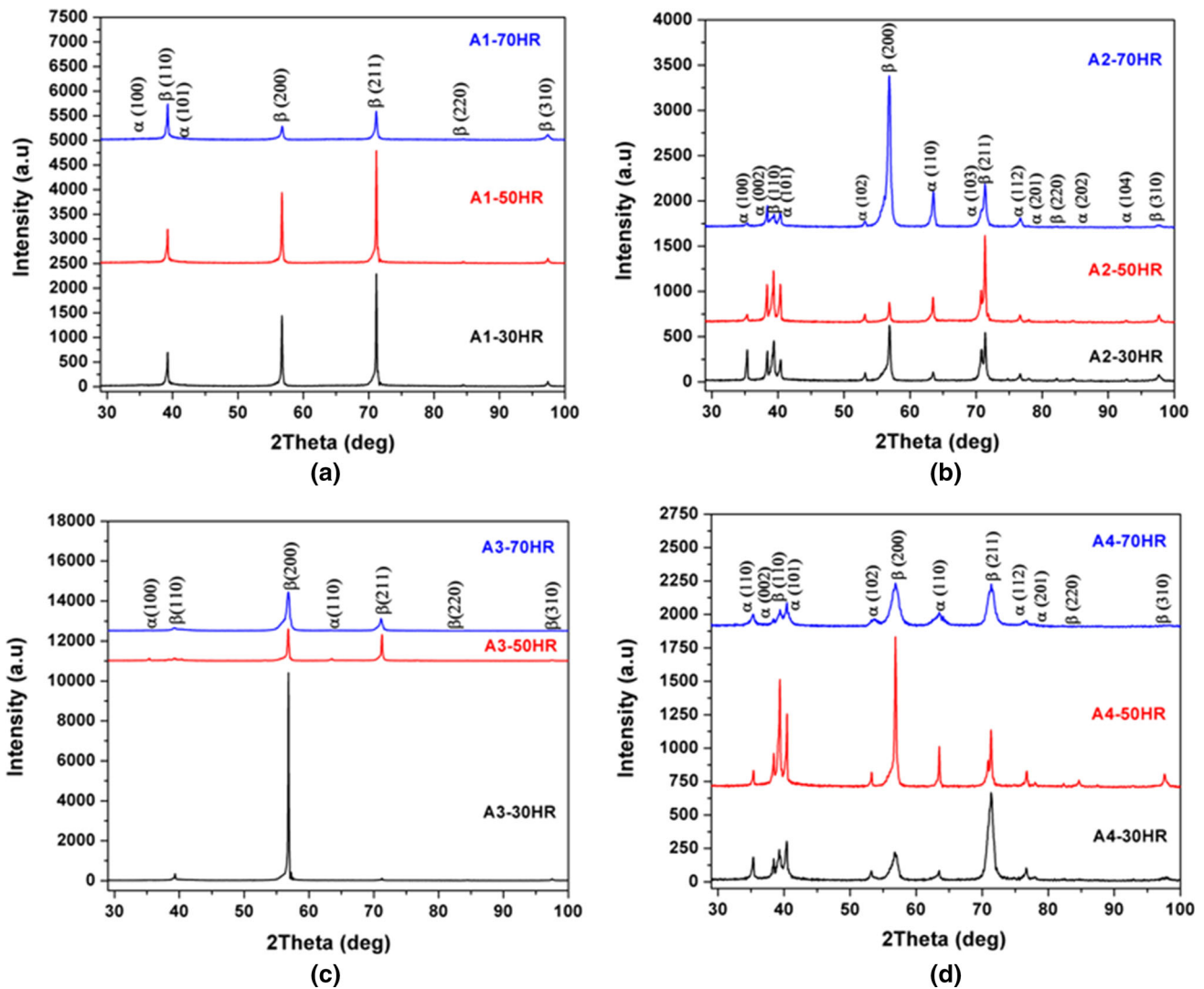


Fig. 2—XRD patterns of the experimental alloys hot rolled to 30, 50, and 70 pct reductions: (a) A1, (b) A2, (c) A3, and (d) A4.

contours in the Euler space defined by three Euler angles ( $\varphi_1$ ,  $\Phi$ ,  $\varphi_2$ ) and typical  $\alpha$ ,  $\gamma$  fibers.

### III. RESULTS

The optical microstructures of all four alloys in as-cast condition are shown in Figures 1(a) through (d). The micrographs exhibit the presence of fine precipitates within and at the prior  $\beta$  grain boundaries. The average grain sizes of the alloys A1, A2, A3, and A4 are 580, 1100, 276, and 750  $\mu\text{m}$ , respectively. The XRD patterns reflect the presence of  $\beta$  phase along with the small amount of  $\alpha$  precipitates (Figure 1(e)). These alloys display strong solidification texture in the as-cast condition (Figure 1(f)).

The XRD patterns of the hot-rolled samples show the presence of  $\beta$  and small amount of  $\alpha$  phase (Figures 2(a) through (d)). The intensities of the  $\alpha$  phase peaks are low

in A1 and A3 in comparison to those of the A2 and A4 alloys indicating the presence of large volume fraction of  $\alpha$  precipitates in the latter. In addition, the intensities of different peaks corresponding to  $\beta$  phase reflections indicate the change in crystallographic texture due to change in both the alloy composition as well as the extent of hot rolling reductions.

The 3D optical microstructures of hot-rolled alloys with different rolling reductions are shown in Figures 3, 5 through 7. The alloy A1 exhibits a systematic change in the microstructure with increasing rolling reductions (Figure 3). It displays two-phase microstructure consisting of continuous film of  $\alpha$  phase along the  $\beta$  grain boundaries (Figures 3(b), (d) and (f)) and fine globular  $\alpha$  phase within the matrix (Figure 4). The aspect ratios of grains increase from 30 to 70 pct reductions. The volume fraction of recrystallized grains (Figure 3(f)) also increases with increase in rolling reductions. In addition, microstructures also reveal the presence of

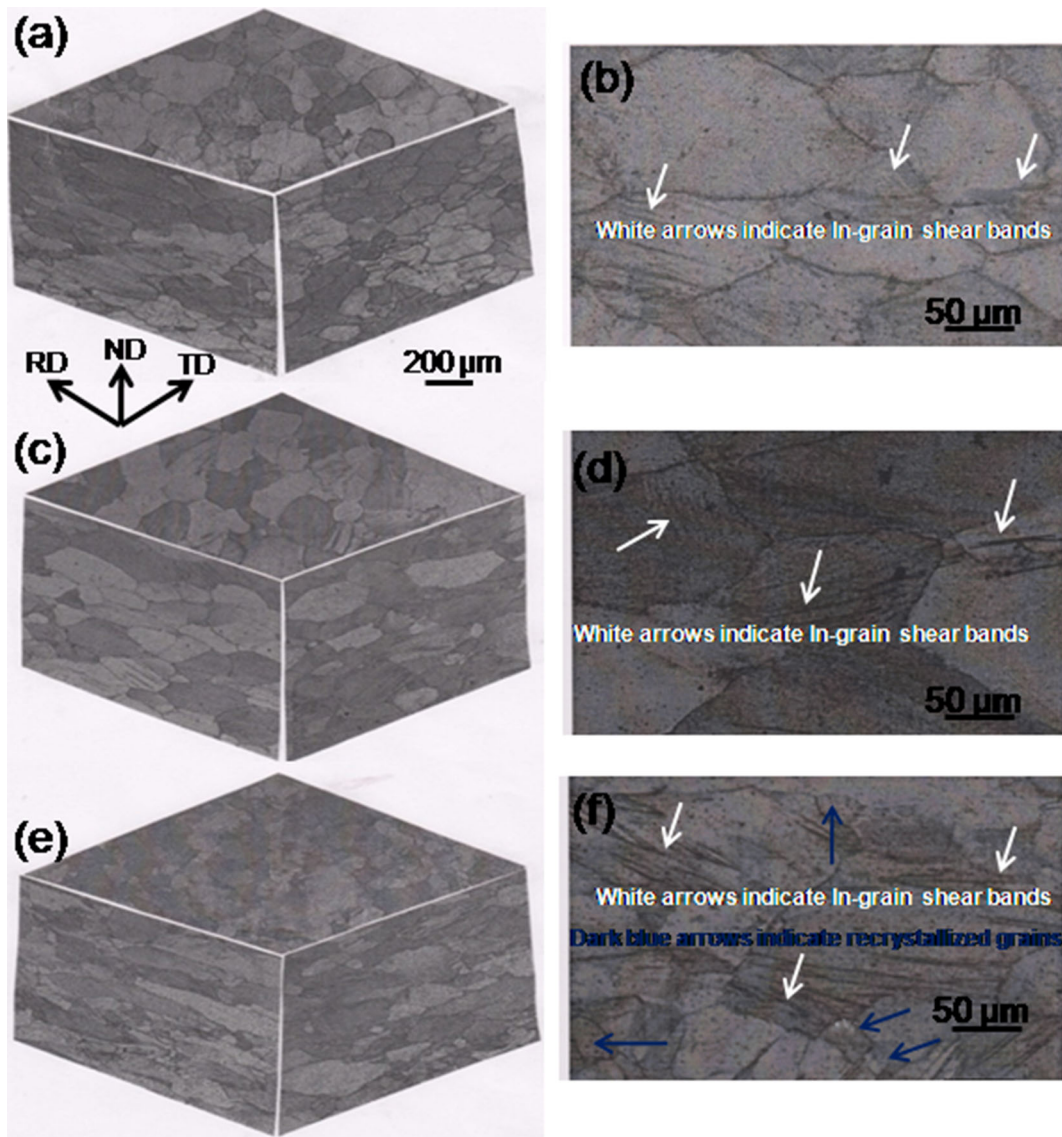


Fig. 3—Optical microstructures of the alloy A1: 30 pct HR (a) 3D low-magnification, (b) high-magnification RD plane, 50 pct HR (c) 3D low-magnification, (d) high-magnification RD plane and 70 pct HR (e) 3D low-magnification, (f) high-magnification RD plane.

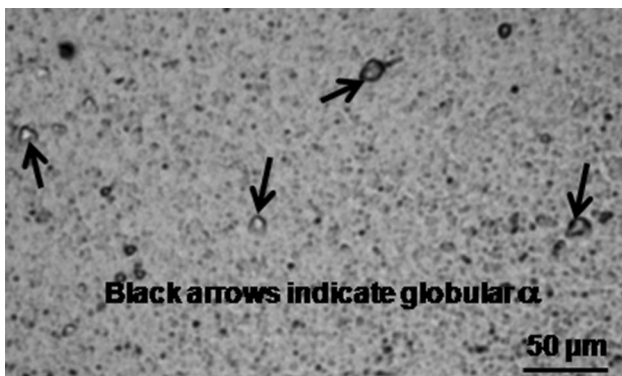


Fig. 4—High-magnification optical microstructure of the alloy A1 in 50 pct HR condition.

in-grain shear bands (Figures 3(b), (d) and (f)) and the fraction of shear bands increases with increase in rolling reductions.

The alloy A2 shows entirely different microstructures from that of the alloy A1. It displays relatively coarse  $\beta$  grains with fine as well as uniform distribution of the  $\alpha$  precipitates (Figure 5). The  $\alpha$  precipitate shows with both globular and elongated morphologies along the rolling direction (Figures 5(b), (d) and (f)). The 70 pct hot-rolled sample clearly shows the formation of banded microstructures (Figure 5(e)). On the other hand, alloy A3 shows elongated grains and the aspect ratios increase with increase in rolling reduction (Figure 6). The extent of recrystallization appears to be less than that of the alloy A1. This alloy also shows the presence of in-grain shear bands (Figures 6(b), (d)

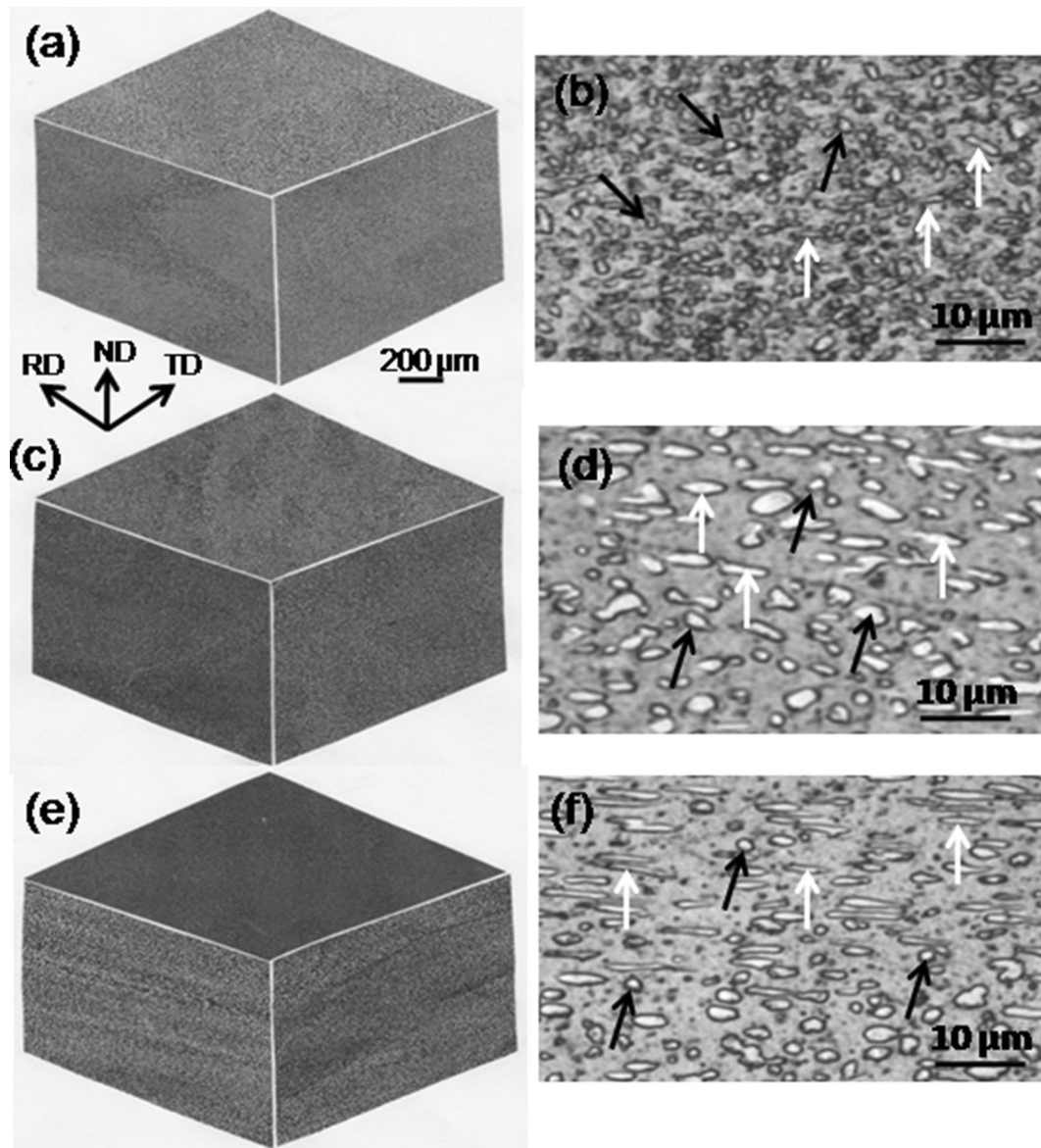


Fig. 5—Optical microstructures of the alloy A2: 30 pct HR (a) 3D low-magnification, (b) high-magnification RD plane, 50 pct HR (c) 3D low-magnification, (d) high-magnification RD plane and 70 pct HR (e) 3D low-magnification, (f) high-magnification RD plane. Black and white arrows indicate globular and elongated  $\alpha$  phase, respectively.

and (f)), and these bands are wavy in 70 pct hot-rolled sample. The microstructures of the alloy A4 exhibit banded features similar to that of the alloy A2 (Figure 7). In addition, it also consists of elongated grains with in-grain shear bands. The high-magnification microstructures reveal the presence of two types of prior beta grains that contain large volume fraction of uniformly distributed  $\alpha$  precipitates with globular and elongated morphology and with the in-grain shear bands with small amount of  $\alpha$  precipitates (Figures 7(e), (f) and (g)). However, the difference between these two types of grains is not very clear in the 30 and 50 pct rolled samples (Figures 7 (a) and (c)).

The evolution of texture in alloy A1 as a function of different hot rolling reductions is shown in Figure 8. The

overall intensity of texture increases from 30 to 50 pct reduction and then decreases in 70 pct hot-rolled sample. The major texture components obtained from the ODFs are  $\{011\}\langle 311 \rangle$  [ $f(g) = 2.5$ ],  $\{011\}\langle 811 \rangle$  [ $f(g) = 2.2$ ],  $\{111\}\langle 110 \rangle$  [ $f(g) = 1.8$ ],  $\{12\ 1\ 1\}\langle 210 \rangle$  [ $f(g) = 1.6$ ],  $\{011\}\langle 100 \rangle$  [ $f(g) = 1.5$ ],  $\{13\ 1\ 5\}\langle 310 \rangle$  [ $f(g) = 1.5$ ],  $\{110\}\langle 114 \rangle$  [ $f(g) = 1.4$ ];  $\{1\ 11\ 13\}\langle 11\ 1\ 0 \rangle$  [ $f(g) = 3.9$ ],  $\{634\}\langle 043 \rangle$  [ $f(g) = 3.3$ ],  $\{011\}\langle 15\ 1\ 1 \rangle$  [ $f(g) = 3.3$ ],  $\{11\ 1\ 13\}\langle 121 \rangle$  [ $f(g) = 3.2$ ],  $\{1\ 11\ 10\}\langle 11\ 1\ 0 \rangle$  [ $f(g) = 3.1$ ],  $\{235\}\langle 320 \rangle$  [ $f(g) = 3.0$ ],  $\{011\}\langle 311 \rangle$  [ $f(g) = 3.0$ ],  $\{001\}\langle 650 \rangle$  [ $f(g) = 2.7$ ],  $\{001\}\langle 740 \rangle$  [ $f(g) = 2.6$ ]; and  $\{345\}\langle 11\ 12\ 3 \rangle$  [ $f(g) = 2.7$ ],  $\{1\ 2\ 13\}\langle 210 \rangle$  [ $f(g) = 2.0$ ],  $\{987\}\langle 2\ 11\ 0 \rangle$  [ $f(g) = 2.0$ ],  $\{8\ 10\ 11\}\langle 132 \rangle$  [ $f(g) = 1.7$ ],  $\{223\}\langle 110 \rangle$  [ $f(g) = 1.6$ ],  $\{221\}\langle 110 \rangle$  [ $f(g) = 1.6$ ] for 30, 50, and 70 pct rolled specimens, respectively.

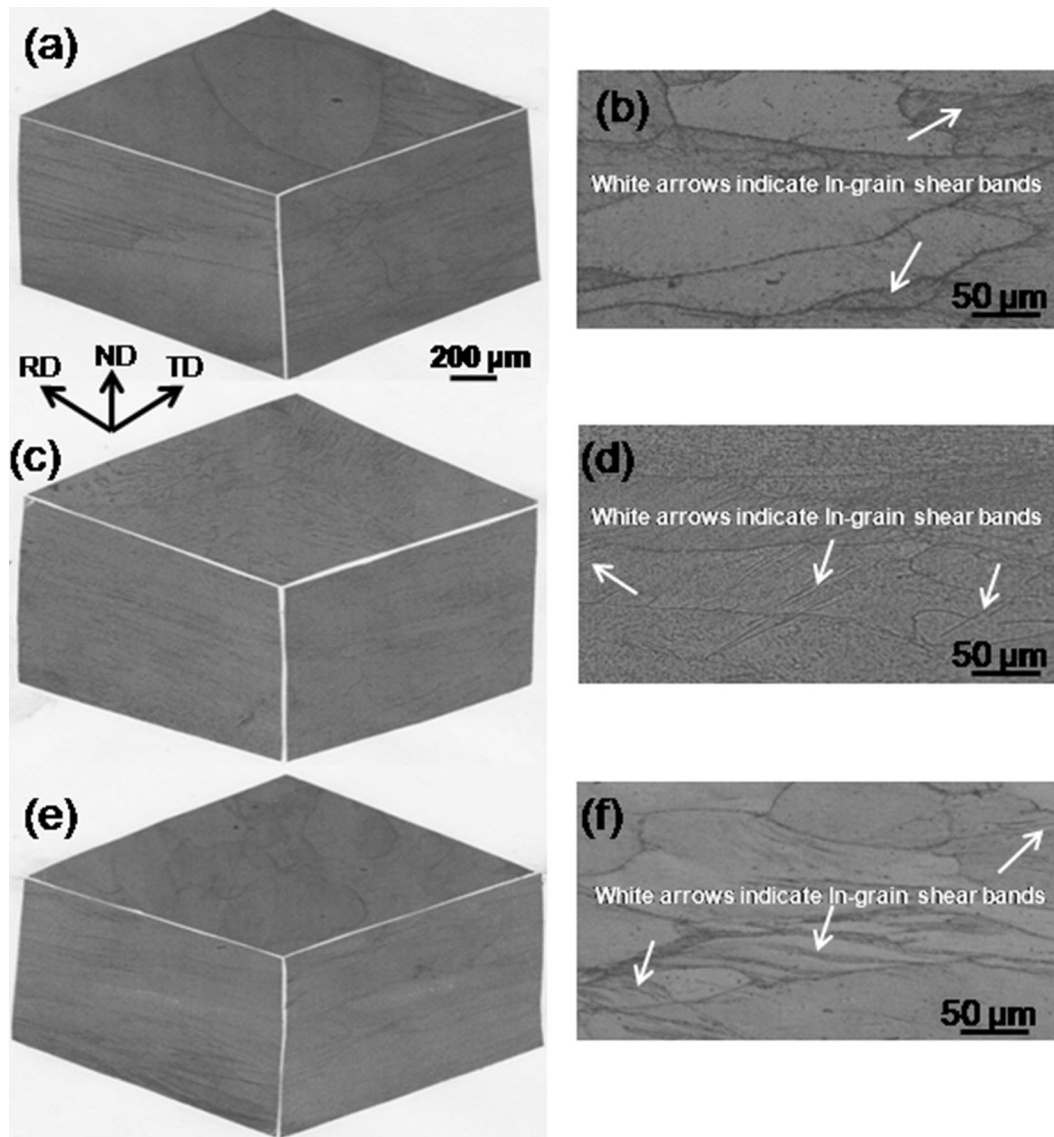


Fig. 6—Optical microstructures of the alloy A3: 30 pct HR (a) 3D low-magnification, (b) high-magnification RD plane, 50 pct HR (c) 3D low-magnification, (d) high-magnification RD plane and 70 pct HR (e) 3D low-magnification, (f) high-magnification RD plane.

The overall intensity of texture of alloy A2 is significantly higher than that of the alloy A1 although it follows similar variation as a function of different rolling reductions (Figure 9). The main texture components obtained from the ODFs are  $\{225\}\langle 110 \rangle$  [ $f(g) = 3.8$ ],  $\{310\}\langle 134 \rangle$  [ $f(g) = 3.7$ ],  $\{11\ 1\ 1\}\langle 011 \rangle$  [ $f(g) = 3.0$ ],  $\{745\}\langle 054 \rangle$  [ $f(g) = 2.9$ ],  $\{11\ 3\ 1\}\langle 2\ 11\ 11 \rangle$  [ $f(g) = 2.4$ ],  $\{345\}\langle 430 \rangle$  [ $f(g) = 2.3$ ],  $\{1\ 3\ 15\}\langle 310 \rangle$  [ $f(g) = 2.2$ ];  $\{1\ 1\ 14\}\langle 110 \rangle$  [ $f(g) = 7.5$ ],  $\{11\ 1\ 1\}\langle 011 \rangle$  [ $f(g) = 6.7$ ],  $\{665\}\langle 110 \rangle$  [ $f(g) = 5.8$ ],  $\{345\}\langle 430 \rangle$  [ $f(g) = 3.8$ ],  $\{767\}\langle 175 \rangle$  [ $f(g) = 3.6$ ],  $\{11\ 2\ 5\}\langle 298 \rangle$  [ $f(g) = 3.2$ ],  $\{3\ 2\ 11\}\langle 141 \rangle$  [ $f(g) = 3.0$ ]; and  $\{1\ 11\ 15\}\langle 110 \rangle$  [ $f(g) = 4.0$ ],  $\{110\}\langle 221 \rangle$  [ $f(g) = 3.8$ ],  $\{113\}\langle 110 \rangle$  [ $f(g) = 3.6$ ],  $\{221\}\langle 110 \rangle$  [ $f(g) = 3.0$ ],  $\{722\}\langle 011 \rangle$  [ $f(g) = 2.8$ ],  $\{12\ 3\ 1\}\langle 166 \rangle$  [ $f(g) = 2.5$ ] for 30, 50, and 70 pct rolled specimens, respectively.

The alloy A3 displays continuous increases in overall intensity with increase in rolling reductions (Figure 10). The main texture components obtained from the ODFs are  $\{355\}\langle 5\ 10\ 7 \rangle$  [ $f(g) = 2.8$ ],  $\{128\}\langle 210 \rangle$  [ $f(g) = 2.6$ ],  $\{11\ 1\ 9\}\langle 253 \rangle$  [ $f(g) = 2.1$ ],  $\{1\ 3\ 12\}\langle 351 \rangle$  [ $f(g) = 2.0$ ],  $\{011\}\langle 10\ 7\ 7 \rangle$  [ $f(g) = 1.8$ ],  $\{011\}\langle 850 \rangle$  [ $f(g) = 1.7$ ],  $\{11\ 11\ 9\}\langle 110 \rangle$  [ $f(g) = 1.7$ ];  $\{10\ 12\ 13\}\langle 132 \rangle$  [ $f(g) = 4.6$ ],  $\{1\ 3\ 15\}\langle 310 \rangle$  [ $f(g) = 3.4$ ],  $\{1\ 2\ 12\}\langle 271 \rangle$  [ $f(g) = 3.2$ ],  $\{001\}\langle 10\ 7\ 0 \rangle$  [ $f(g) = 3.1$ ],  $\{118\}\langle 110 \rangle$  [ $f(g) = 2.7$ ],  $\{557\}\langle 223 \rangle$  [ $f(g) = 2.5$ ],  $\{165\}\langle 111 \rangle$  [ $f(g) = 2.3$ ],  $\{3\ 1\ 15\}\langle 361 \rangle$  [ $f(g) = 2.2$ ],  $\{112\}\langle 110 \rangle$  [ $f(g) = 2.0$ ]; and  $\{557\}\langle 110 \rangle$  [ $f(g) = 10.6$ ],  $\{7\ 7\ 10\}\langle 110 \rangle$  [ $f(g) = 10.3$ ],  $\{001\}\langle 650 \rangle$  [ $f(g) = 7.6$ ],  $\{001\}\langle 870 \rangle$  [ $f(g) = 7.6$ ],  $\{115\}\langle 110 \rangle$  [ $f(g) = 7.0$ ],  $\{1\ 1\ 15\}\langle 110 \rangle$  [ $f(g) = 6.6$ ],  $\{001\}\langle 750 \rangle$  [ $f(g) = 5.9$ ],  $\{001\}\langle 15\ 14\ 0 \rangle$  [ $f(g) = 5.8$ ],  $\{611\}\langle 011 \rangle$  [ $f(g) = 4.6$ ],  $\{10\ 1\ 1\}\langle 011 \rangle$  [ $f(g) = 4.6$ ],  $\{14\ 2$

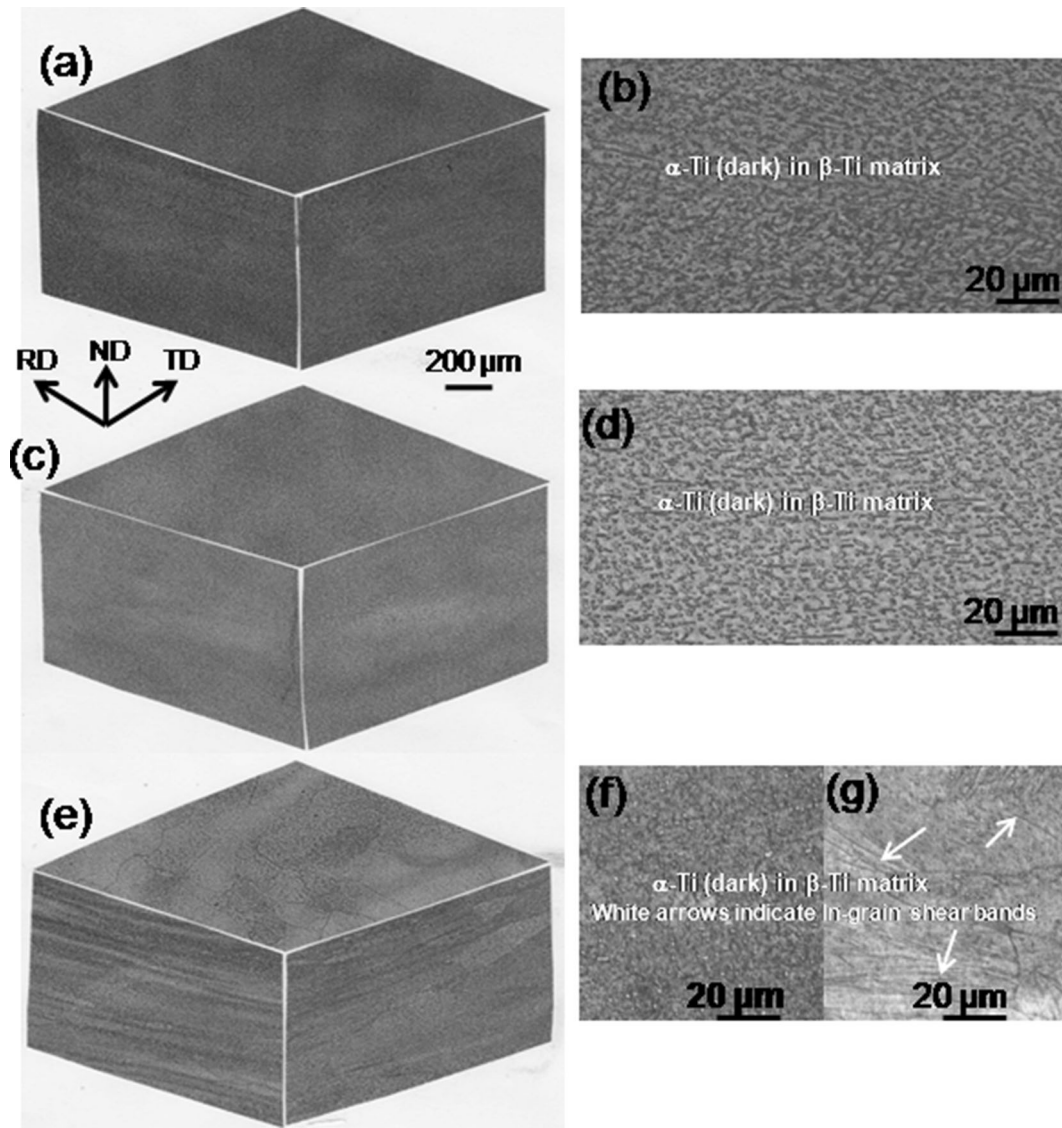


Fig. 7—Optical microstructures of the alloy A4: 30 pct HR (a) 3D low-magnification, (b) high-magnification RD plane, 50 pct HR (c) 3D low-magnification, (d) high-magnification RD plane and 70 pct HR (e) 3D low-magnification, (f) high-magnification RD plane, and (g) high-magnification RD plane taken from different locations showing in-grain shear bands.

$1\}\langle 1\ 12\ 10\rangle$  [ $f(g) = 4.2$ ],  $\{479\}\langle 737\rangle$  [ $f(g) = 3.9$ ] for 30, 50, and 70 pct rolled specimens, respectively.

The overall intensity of texture of alloy A4 marginally decreases in 50 pct rolled specimen and then slightly increases in 70 pct rolled sample (Figure 11). The main texture components obtained from the ODFs are  $\{4\ 11\ 14\}\langle 11\ 4\ 0\rangle$  [ $f(g) = 2.3$ ],  $\{1\ 5\ 11\}\langle 352\rangle$  [ $f(g) = 2.1$ ],  $\{656\}\langle 101\rangle$  [ $f(g) = 2.0$ ],  $\{11\ 1\ 3\}\langle 176\rangle$  [ $f(g) = 2.0$ ],  $\{335\}\langle 110\rangle$  [ $f(g) = 1.9$ ],  $\{001\}\langle 650\rangle$  [ $f(g) = 1.8$ ],  $\{001\}\langle 7\ 10\ 0\rangle$  [ $f(g) = 1.8$ ],  $\{1\ 1\ 15\}\langle 110\rangle$  [ $f(g) = 1.7$ ],  $\{1\ 1\ 15\}\langle 110\rangle$  [ $f(g) = 2.6$ ],  $\{118\}\langle 110\rangle$  [ $f(g) = 2.6$ ],  $\{1\ 2\ 13\}\langle 210\rangle$  [ $f(g) = 2.6$ ],  $\{4\ 11\ 10\}\langle 11\ 4\ 0\rangle$  [ $f(g) = 2.1$ ],  $\{11\ 11\ 13\}\langle 110\rangle$  [ $f(g) = 1.8$ ],  $\{112\}\langle 110\rangle$  [ $f(g) = 1.8$ ],  $\{578\}\langle 132\rangle$  [ $f(g) = 1.7$ ],  $\{211\}\langle 1\ 13\ 11\rangle$  [ $f(g) = 1.7$ ]; and  $\{1\ 1\ 15\}\langle 110\rangle$  [ $f(g) = 4.0$ ],  $\{1\ 1\ 11\}\langle 011\rangle$  [ $f(g) = 4.0$ ],  $\{557\}\langle 110\rangle$  [ $f(g) = 3.0$ ],  $\{1\ 11\ 1\}\langle 11\ 2\ 11\rangle$  [ $f(g) = 3.0$ ],  $\{118\}\langle 110\rangle$  [ $f(g) = 2.9$ ],  $\{115\}\langle 110\rangle$

[ $f(g) = 2.9$ ],  $\{433\}\langle 011\rangle$  [ $f(g) = 2.8$ ],  $\{311\}\langle 011\rangle$  [ $f(g) = 2.8$ ],  $\{225\}\langle 110\rangle$  [ $f(g) = 2.8$ ],  $\{114\}\langle 110\rangle$  [ $f(g) = 2.4$ ] for 30, 50, and 70 pct rolled specimens, respectively.

The ODF plots display two well-known orientations spread which are in turn described as  $\alpha$  and  $\gamma$  fiber plots. The intensity maxima in  $\alpha$  and  $\gamma$  fibers are at  $\{001\}\langle 110\rangle$ ,  $\{112\}\langle 110\rangle$ ,  $\{111\}\langle 110\rangle$ ,  $\{110\}\langle 110\rangle$ , and  $\{111\}\langle 110\rangle$ ,  $\{111\}\langle 112\rangle$ , respectively. The overall intensities of the  $\alpha$  fiber of alloys A1 and A2 increase from 30 to 50 pct rolling reductions and then decrease in 70 pct hot-rolled specimen (Figure 12). On the other hand, the intensities of  $\alpha$  fiber of alloys A3 and A4 are nearly same up to 50 pct reduction and then exhibit overall increase in 70 pct hot-rolled sample (Figure 12). The overall intensity of  $\gamma$  fiber of alloys A1 and A2 shows a significant increase from 30 to 50 pct rolling reductions and then it



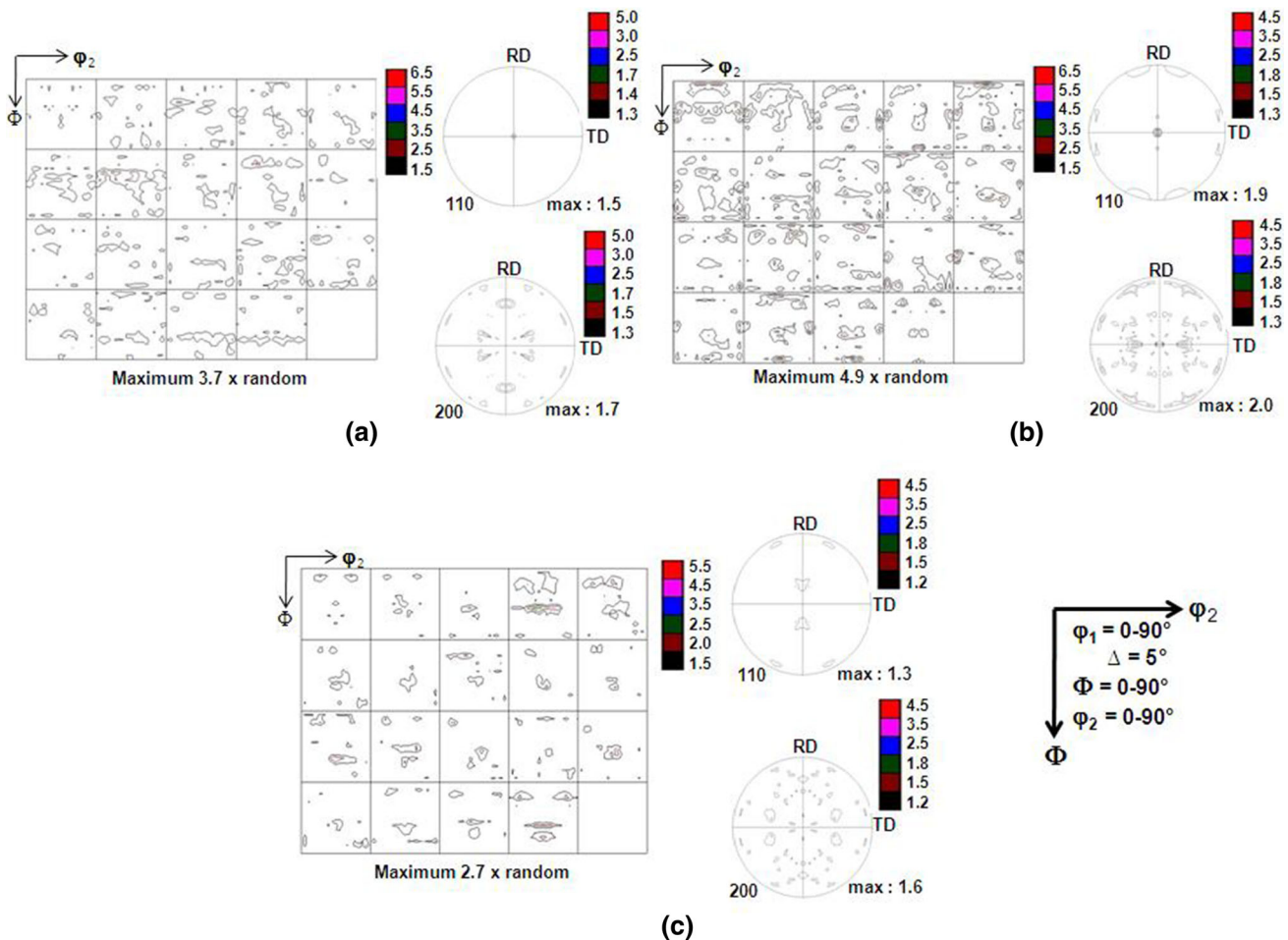


Fig. 8—Texture of the alloy A1 in (a) 30 pct, (b) 50 pct, and (c) 70 pct HR conditions.

shows sharp decrease in 70 pct rolled specimen. In contrast, overall intensity of  $\gamma$  fiber of alloy A3 continuously increases with increase in rolling reduction. In alloy A4, it reflects a marginal decrease from 30 to 50 pct and then increases for 70 pct rolling reductions (Figure 13).

#### IV. DISCUSSION

The as-cast alloys exhibit the presence of fine  $\alpha$  phase precipitates in  $\beta$  matrix. This is because of solidification and the phase transformations associated during melting and subsequent cooling. The solidification reaction can be written as  $L \rightarrow L + \beta \rightarrow \beta \rightarrow \beta + \alpha$ . The presence of  $\alpha$  precipitates in the  $\beta$  matrix is due to solid state transformation. The microstructures of the as-cast alloys display different sizes of prior  $\beta$  grains, formation of subgrains during solidification, and different volume fractions of  $\beta$  and  $\alpha$  phases. The prior  $\beta$  grain sizes of alloys A1 and A3 are finer than those of A2 and A4. The formation of subgrains has been reported in Ti-5553 alloy, and this has been attributed either due to the

strains associated with  $\beta$  to  $\alpha$  phase transformation<sup>[19]</sup> or polygonization through static recovery occurring during cooling.<sup>[22]</sup> The variation in the microstructures of the as-cast alloys can therefore be attributed to the presence of different amounts of alloying elements. This in turn decides the volume fractions of  $\beta$  and  $\alpha$  phases as well as the  $\beta$  transus temperature.

The XRD patterns and (110) pole figures of the as-cast alloys exhibit the formation of sharp {110} texture (Figures 1(e) and (f)). The location of main texture component is close to the center of pole figure in alloys A1 and A3, while it is shifted from the center in A2 and A4. This can be attributed to the presence of large volume fraction of  $\alpha$  precipitate phase in alloys A2 and A4 in comparison to those of the A1 and A3 (Figures 2(a) through (d)). The presence of larger amount of the  $\alpha$  phase appears to prevent the development of perfect (110) orientation during solidification.

3D optical microstructures of the hot-rolled alloys display different features in terms of grain morphology as well as recrystallized grains. A comparison of the microstructures of alloy A1 in hot-rolled condition with the as-cast clearly indicates that the material is

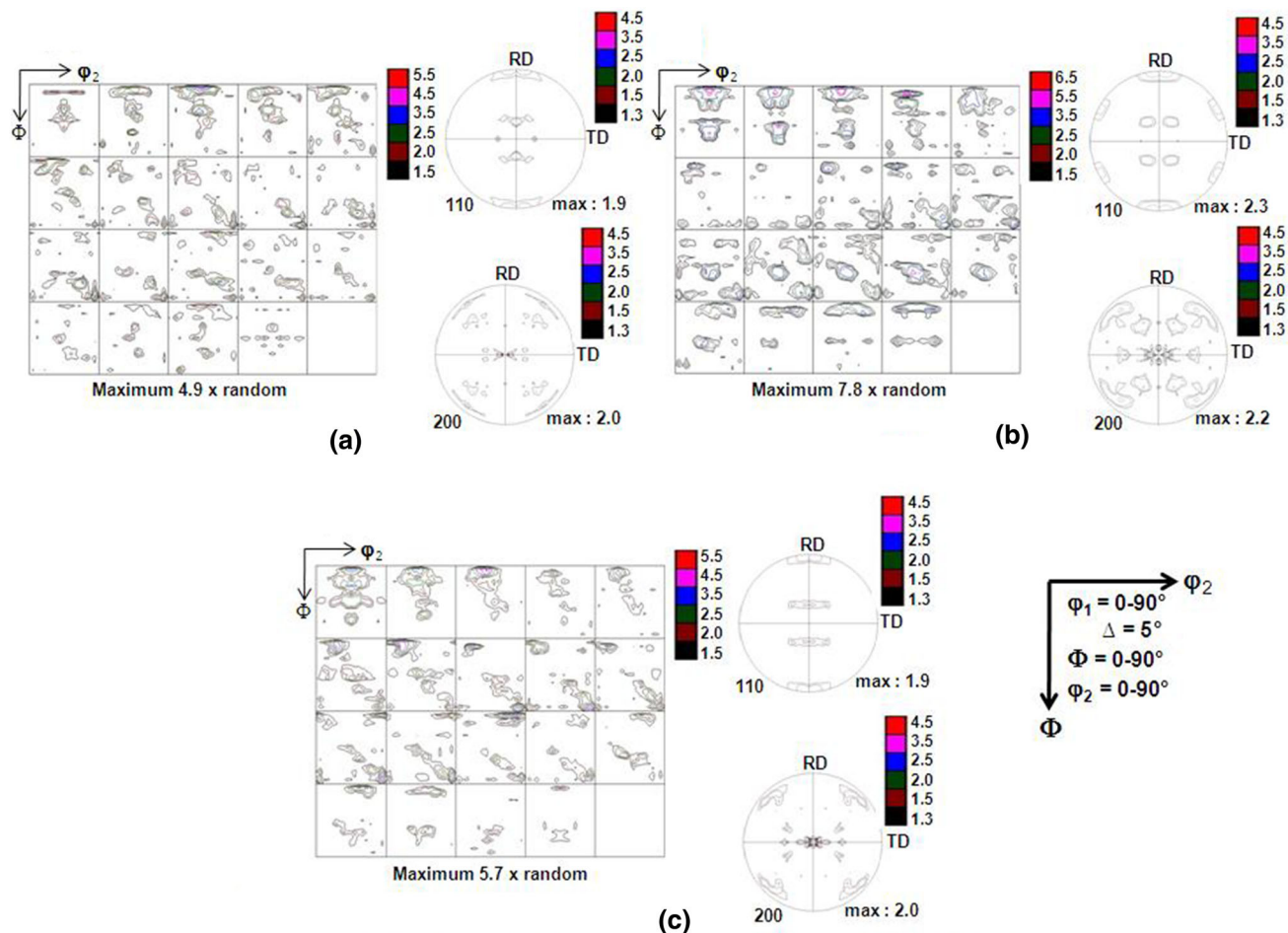


Fig. 9—Texture of the alloy A2 in (a) 30 pct, (b) 50 pct, and (c) 70 pct HR conditions.

completely recrystallized during hot rolling (Figures 1 and 3). The 70 pct hot-rolled sample consists of elongated grains with very high aspect ratio as well as fine equiaxed grains. The development of this microstructure is associated with two steps: (i) the sizes of recrystallized grains formed during 30 and 50 pct rolled samples increase and further elongate during 70 pct rolling reduction and (ii) nucleation of new grains occurs during dynamic recrystallization. In addition, hot rolling deformation also introduces in-grain shear bands due to inhomogeneous deformation. The 3D microstructures of the alloy A3 appear to be similar to that of the alloy A1; however, alloy A3 does not show fine equiaxed grains (Figure 6). All the grains of 70 pct hot-rolled specimen are elongated. In addition, a few elongated grains display (Figure 6(f)) large number of sides.

The microstructures of the alloys A2 (Figure 5) are quite different than those of the alloys A1 and A3. These are banded microstructures with very high aspect ratios formed by elongated prior  $\beta$  grains. Very fine distribution of  $\alpha$  precipitate phase with globular and elongated morphology within the matrix is shown in Figures 5(b), (d) and (f). The extent of elongation of  $\alpha$  precipitates

increases with increase in rolling reductions of both the alloys (Figures 5(b), (d) and (f)). The banded features within the prior  $\beta$  grains consist of even distribution of  $\alpha$  precipitates with both the morphologies as mentioned above (Figures 5(b) through (f)). In contrast, the microstructures of alloy A4 display banded types of features similar to that of the alloy A2; however, they exhibit two types of the prior  $\beta$  grains consisting of uniform distributions of  $\alpha$  precipitates and in-grain shear bands (Figure 7). Therefore, the microstructures of alloy A4 consist of the features of alloys A1/A3 and A2. It is difficult to comment about the recrystallization behavior of the A2 and A4 alloys based on the optical microstructures.

The microstructures of the alloy A1 in 70 pct hot-rolled condition are also supported by band contrast and grain boundary map images (Figures 14(a) and (b)) obtained by EBSD technique. The microstructure displays both the elongated and fine equiaxed grains. As mentioned above, the former is associated with the deformation of the equiaxed recrystallized grains and recovery, while the latter is related with recrystallization. The grain boundary image of this specimen (Figure 14(b)) distinctively reflects three types of grain

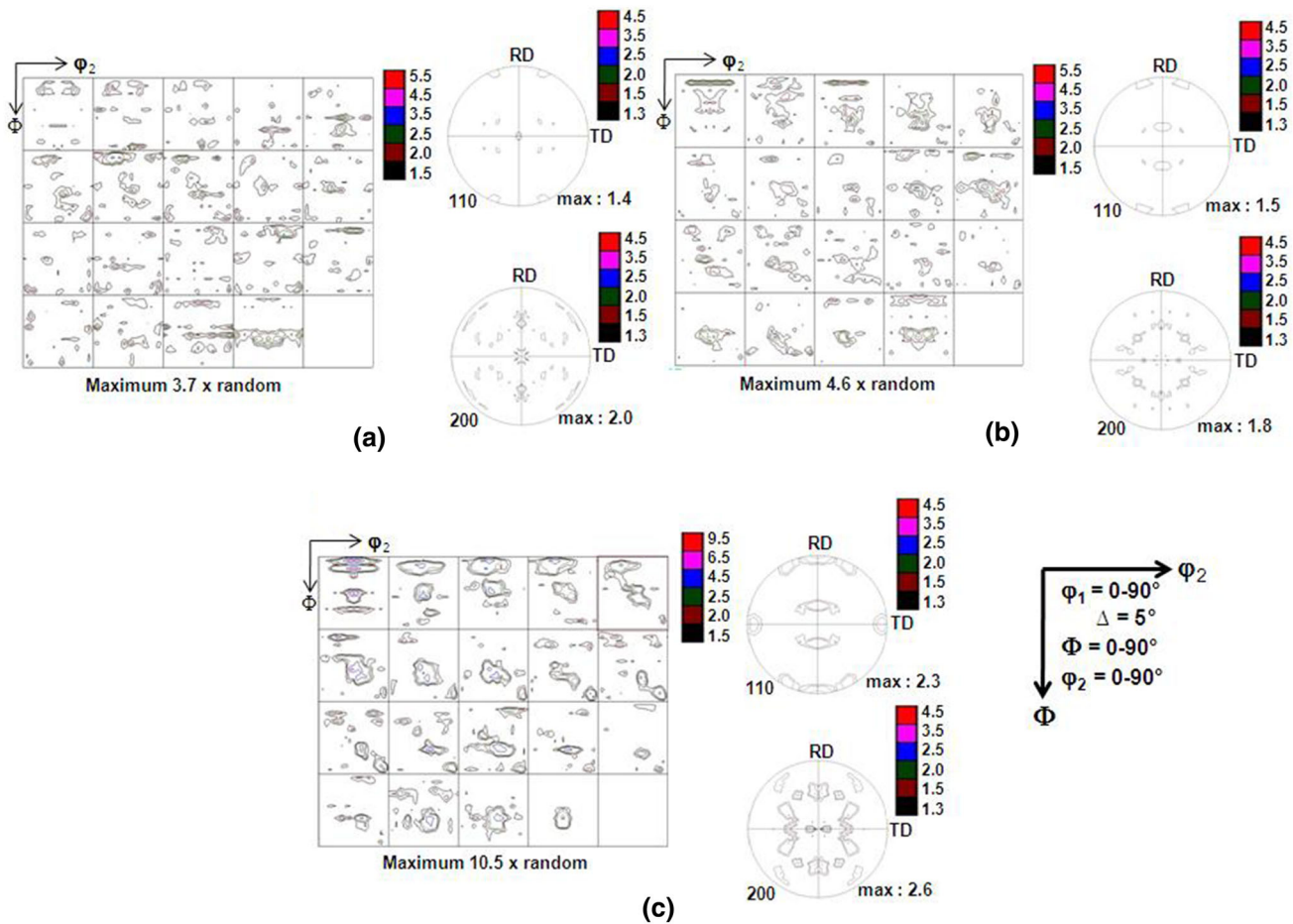


Fig. 10—Texture of the alloy A3 in (a) 30 pct, (b) 50 pct, and (c) 70 pct HR conditions.

boundaries namely 2 to 10 deg (green), 10 to 15 deg (red), and >15 deg (blue). The 2 to 10 deg (green) and 10 to 15 deg (red) boundaries belong to in-grain shear bands. On the other hand, all the grain boundaries having >15 deg (blue) are the result of the subsequent stages of deformation as well as recovery/recrystallization during hot rolling.

In order to understand the evolutions of microstructure of alloy A2, band contrast image and grain boundary map have been obtained by EBSD (Figures 15(a) and (b)) and corresponding distribution of  $\alpha$  phase is shown in Figure 15(c). The grain boundary map of this specimen indicates the presence of three types of boundaries, *i.e.*, 2 to 10 deg (green), 10 to 15 deg (red), and >15 deg (blue) in  $\beta$  matrix. The volume fractions of the 2 to 10 deg boundaries are largest which belong to subgrains. These have probably appeared after recovery during final stage of hot rolling. In contrast, 10 to 15 deg (red) and >15 deg (blue) boundaries are related with initial stage of recrystallization (appearing during the last stage of hot rolling) and earlier recrystallized grains, respectively. A comparison of microstructures of alloys A1 and A2 obtained by EBSD reflects that the kinetics of recrystallization is faster in alloy A1 than that of the A2 (Figures 16(a) through (c)).

The difference in microstructures of the alloys A1 and A2 can therefore be attributed to the large volume fraction of the  $\alpha$  phase which has appeared due to low Mo and high V contents, respectively, in A2. The  $\alpha$  phase in turn retards the recrystallization kinetics in alloy A2 which shows a large volume fraction of low-angle grain boundaries (2 to 10 deg). As mentioned above, microstructure of alloy A4 consists of both the features of the alloys A1 and A2. Although the Mo contents of alloy A2 and A4 are same, it appears that a combined effect of V and Cr results in a mixed microstructure having features of both the alloys, *i.e.*, A1 and A2 in A4. It also appears that the formation of in-grain shear bands in the alloys being investigated depends on a critical volume fraction of the  $\alpha$  phase which in turn is related to the Mo content. Therefore, higher Mo content with low volume fraction of  $\alpha$  phase exhibits the presence of in-grain shear bands within the  $\beta$  grains (alloys A1 and A3), while large volume fraction of  $\alpha$  phase acts as a recrystallization inhibitor.

The alloys A1 and A3 exhibit the presence of in-grain shear bands (Figures 3 and 6). Formation of in-grains shear bands has been reported in bcc and fcc materials during hot, warm, and cold rolling in addition to dynamic deformation modes by several investigators.<sup>[25–28]</sup>

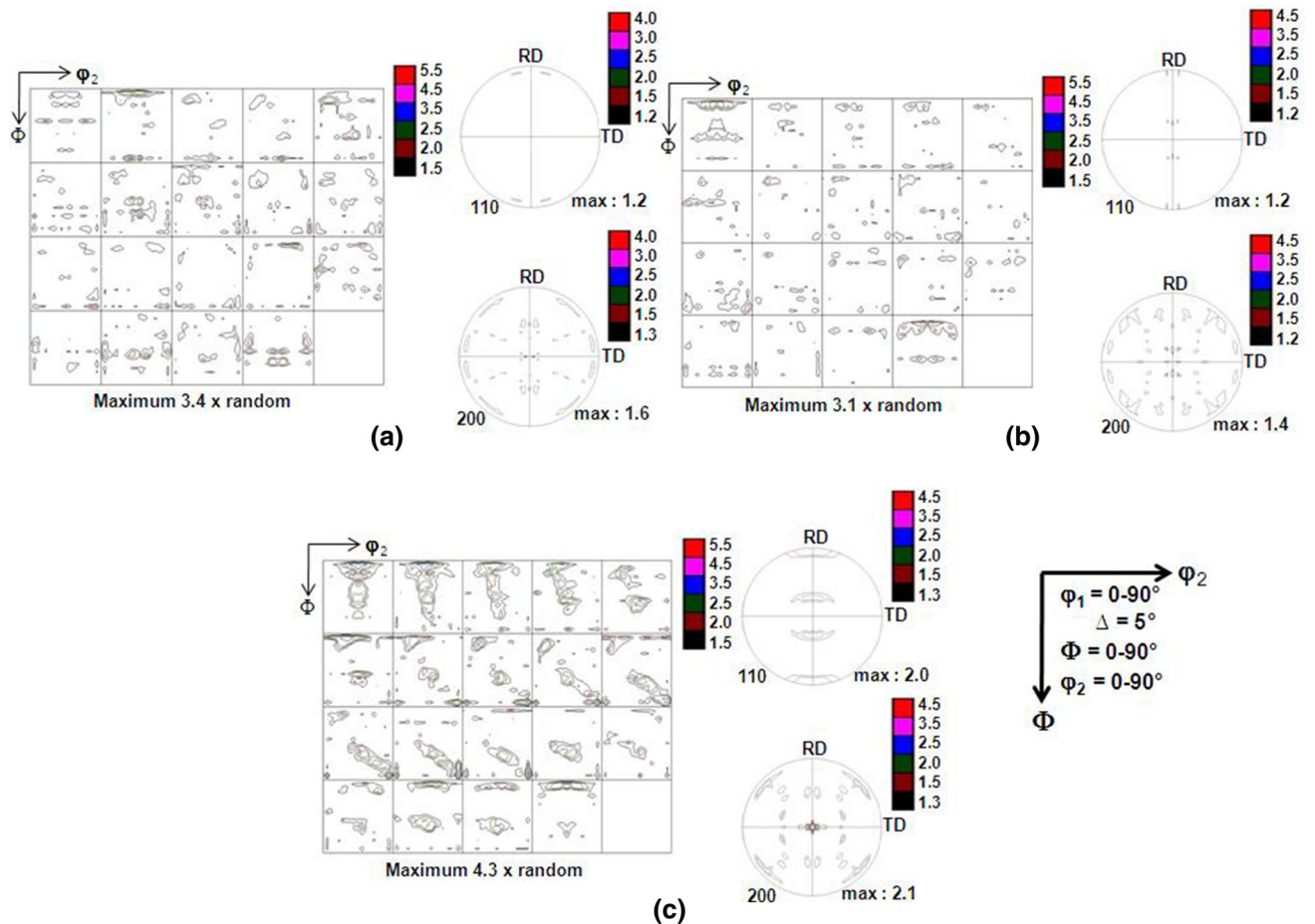


Fig. 11—Texture of the alloy A4 in (a) 30 pct, (b) 50 pct, and (c) 70 pct HR conditions.

These bands correspond to thin region of intense shear that occurs independently of both the grain structure as well as the normal crystallographic consideration. The shear bands are a form of plastic instability and occur during plain strain deformation such as rolling. They appear in cold-rolled materials at  $\sim 35$  deg to the rolling plane and parallel to the transverse direction.<sup>[29]</sup> However, the appearance of shear bands is different in different processing conditions as mentioned above.

Formation of shear bands depends on several factors such as grain size and orientation, solute content and deformation temperature, stacking fault energy (SFE), and strain hardening exponent.<sup>[29]</sup> The observations of shear bands in the present alloys are therefore due to large  $\beta$  grain size and associated orientation, solute contents (different amounts of alloying elements), hot rolling temperature, and low values of strain hardening exponent. Shear bands formation has been recently reported in the present experimental alloys in WQ condition during Vickers indentation.<sup>[30]</sup> On the other hand, furnace-cooled materials having large volume fraction of  $\alpha$ -titanium (hcp) phase do not exhibit the

presence of shear bands. This has been attributed to high value of strain hardening exponent associated with  $\alpha$  phase in comparison to that of the  $\beta$ . This also explains the absence of in-grain shear bands in alloys A2 and in some grains of alloy A4 having large volume fraction of the  $\alpha$  phase. It is to be noted that some of the grains of alloy A4 consist of in-grain shear bands along with small volume fraction of the  $\alpha$  precipitates similar to those of the alloys A1 and A3, while some of the grains exhibit similar features to that of the alloy A2 having large volume fraction of  $\alpha$  precipitates with globular and elongated morphologies. It appears that both the prior  $\beta$  grains mentioned above behave differently during hot rolling.

The development of textures during hot rolling of present alloys is different in terms of overall intensity and major components. The alloys A1 and A2 exhibit increase in overall intensity from 30 to 50 pct rolling reductions and then decrease in intensity from 50 to 70 pct rolling reductions. In contrast, the alloy A3 shows a continuous increase in intensity with increase in rolling reduction, while in alloy A4, intensity decreases from 30 to 50 pct and then increases in 70 pct rolled

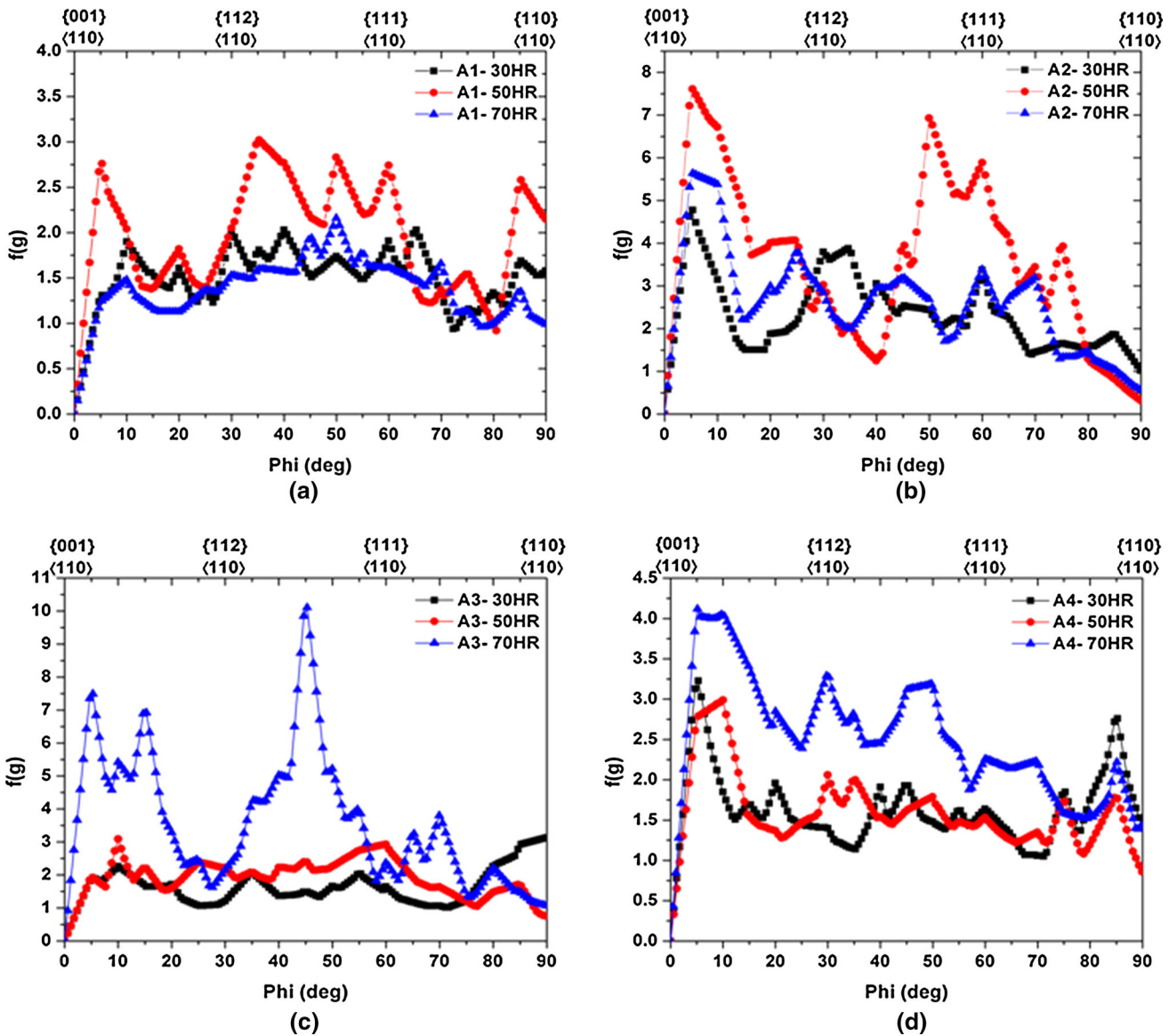


Fig. 12— $\alpha$  fibers of the hot-rolled alloys: (a) A1, (b) A2, (c) A3, and (d) A4.

sample. It is to be noted here that the hot rolling process consists of both the deformation as well as the recrystallization components. The variation of overall intensity in the present alloys can therefore be attributed to the extent of solid solution in the  $\beta$  matrix and the presence of second phase ( $\alpha$ ) due to different amounts of alloying elements. The decrease in intensity indicates control of recrystallization components, while increase in intensity indicates that the deformation components dominate.

The normal rolling textures in bcc metals and alloys such as Fe, Mo, Ta, Nb, V, low carbon steel, and ferritic stainless steels have  $\{111\}\langle 112\rangle$ ,  $\{111\}\langle 123\rangle$ ,  $\{001\}\langle 110\rangle$ ,  $\{112\}\langle 110\rangle$ , and  $\{111\}\langle 110\rangle$  orientations.<sup>[31–34]</sup> The development of texture during rolling and recrystallization can also be described in terms of intensity variation in  $\alpha$  and  $\gamma$  fibers. The orientation intensity along the  $\alpha$

fiber increases up to 70 pct reductions, but with further rolling, components  $\{112\}\langle 110\rangle$  and  $\{111\}\langle 110\rangle$  become more prominent. The  $\gamma$  fiber is uniform up to 80 pct reduction, but thereafter  $\{111\}\langle 110\rangle$  component sharpens. On the other hand, there is a loss of intensity near  $\{112\}\langle 110\rangle$ ,  $\{001\}\langle 110\rangle$  and an increase in strength of the  $\{111\}\langle 112\rangle$  component in  $\alpha$  and  $\gamma$  fibers during recrystallization, respectively. The  $\{111\}\langle 110\rangle$  component remains constant.<sup>[31–34]</sup>

As mentioned above, hot-rolled samples consist of both the deformation as well as the recrystallization components. Texture components observed in present alloys belong to both the rolling and recrystallization orientations; however, they lie either at or near stable end orientations in both the cases. This can also be clearly seen in corresponding  $\alpha$  and  $\gamma$  fibers (Figures 12 and 13), wherein the intensities of components are

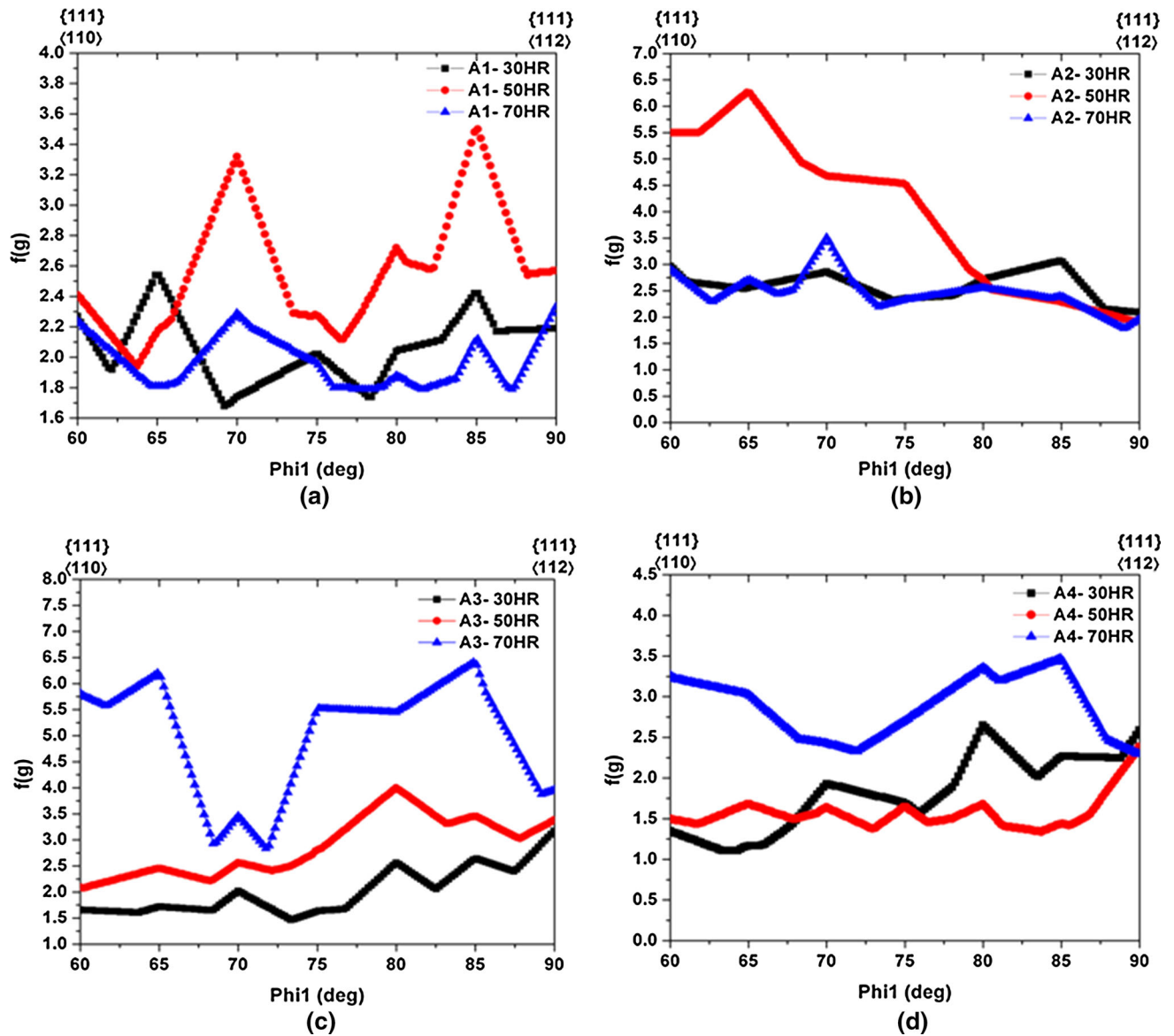


Fig. 13— $\gamma$  fibers of the hot-rolled alloys: (a) A1, (b) A2, (c) A3, and (d) A4.

shifted from typical maxima locations. This can be attributed to amount of deformation as well as dynamic recrystallization during hot rolling which are probably not sufficient to produce stable end orientations.

As mentioned above, the orientation intensities in the  $\alpha$  fiber in alloy A1 exhibit an increase in orientation intensity from 30 to 50 pct rolling reduction (Figure 12). This also reflects the sharpening of rolling components  $\{112\}\langle 110\rangle$  and  $\{111\}\langle 110\rangle$  which is typical characteristics of rolling textures. On the other hand, 70 pct rolled sample shows overall weakening of the  $\alpha$  fiber. Similarly, the overall intensity of the  $\gamma$  fiber increases from 30 to 50 pct and then decreases from 50 to 70 pct reductions. The intensity of the  $\{111\}\langle 110\rangle$  component remains nearly constant for all the three reductions. Therefore, development of texture in alloy A1 can be attributed to the domination of rolling texture from 30 to 50 pct and

then supremacy of recrystallization texture from 50 to 70 pct rolling reductions. This observation is in agreement with the variation of overall intensities in corresponding ODFs (Figure 8) and the presence of large volume fraction of recrystallized grains (Figure 3) and high-angle grain boundaries ( $>15$  deg) in 70 pct hot-rolled sample (Figure 14).

The  $\alpha$  fiber of the alloy A2 displays similar variation to that of the alloy A1 from 30 to 50 pct hot rolling deformation. This shows increase in intensities between  $\{112\}\langle 110\rangle$  and  $\{111\}\langle 110\rangle$  and near  $\{111\}\langle 110\rangle$  orientations. The  $\gamma$  fiber exhibits a sharp increase in intensity of  $\{111\}\langle 110\rangle$  orientation. These are the typical characteristics of deformation texture. Further rolling up to 70 pct reduction reduces the overall intensity of the  $\alpha$  and  $\gamma$  fibers. However, the  $\{112\}\langle 110\rangle$  and  $\{001\}\langle 110\rangle$  orientations display similar and nearly one-fourth

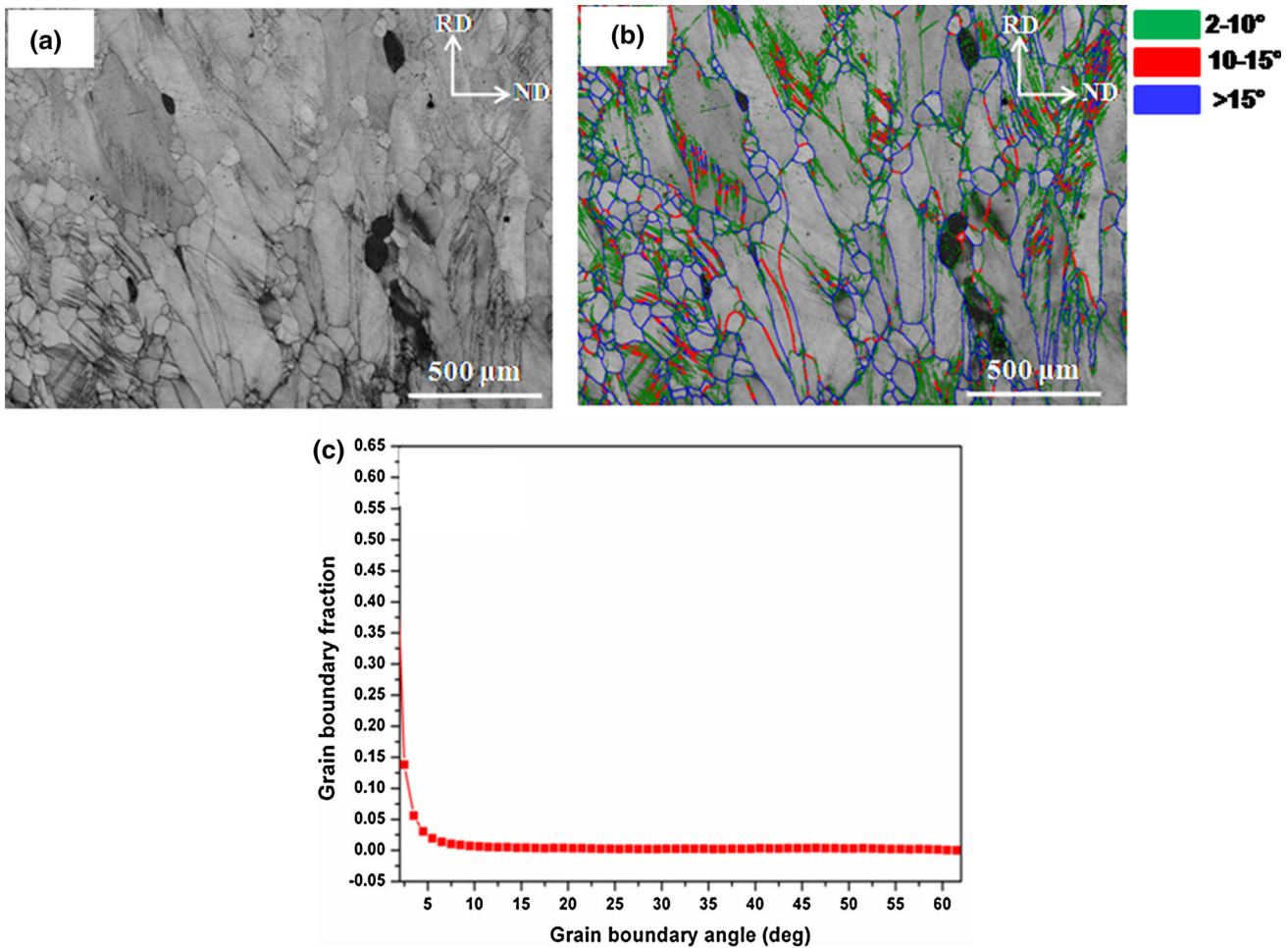


Fig. 14—Microstructures of the 70 pct hot-rolled alloy A1 (a) band contrast, (b) grain boundary map, and (c) grain boundary distribution obtained by EBSD technique (Color figure online).

reduction in intensity, respectively. On the other hand, the  $\{111\}\langle 112\rangle$  component displays almost no change in intensity from 50 to 70 pct reductions. This clearly indicates that the extent of recrystallization is quite less in this alloy, and corresponding sample displays banded microstructure (Figure 5). The presence of large volume fraction of 2 to 10 deg grain boundaries (Figure 15) associated with subgrains also supports the evolution of texture during hot rolling of alloy A2.

As mentioned above, the overall intensity of alloy A3 increases with increase in rolling reductions although the increase is marginal from 30 to 50 pct and sharp from 50 to 70 pct rolling reductions. Both the  $\alpha$  and  $\gamma$  fibers exhibit the similar changes. The  $\{112\}\langle 110\rangle$  and  $\{111\}\langle 110\rangle$  orientations show a marginal increase in intensity in  $\alpha$  fiber, while the  $\{111\}\langle 110\rangle$  component also reflects slight increase in intensity in  $\gamma$  fiber. On contrary, an orientation between  $\{112\}\langle 110\rangle$  and  $\{111\}\langle 110\rangle$  location exhibits a sharp increase in intensity in 70 pct rolled sample. The intensity of  $\{111\}\langle 110\rangle$  orientation also increases sharply in the  $\gamma$  fiber. This clearly reflects that the deformation components prevail from 30 to 70 pct rolling reductions. As a result, only few recrystallized grains are observed in 70 pct hot-rolled sample of the alloy A3 (Figure 6).

tallized grains are observed in 70 pct hot-rolled sample of the alloy A3 (Figure 6).

The overall intensity variation of alloy A4 shows different patterns than those of alloys A1, A2, and A3. It decreases marginally from 30 to 50 pct and then increases from 50 to 70 pct reductions. This shows a slight loss of intensity near  $\{112\}\langle 110\rangle$ , while there is no change in intensity of  $\{111\}\langle 110\rangle$  and  $\{111\}\langle 112\rangle$  orientations in the  $\alpha$  and  $\gamma$  fibers. This indicates softening of texture due to recovery or early stage of recrystallization. On the other hand, 70 pct rolled sample exhibits overall increase in intensity of  $\alpha$  and  $\gamma$  fibers with sharpening of rolling components. Therefore, texture present in 70 pct rolled sample consists mainly of the deformation components with banded microstructure (Figure 7).

The difference in evolution of microstructures and textures of the present alloys in terms of grain size and morphology of the  $\beta$  grains, volume fraction and morphology of  $\alpha$  precipitates within  $\beta$  matrix, extent of recrystallization, and formation of in-grain shear bands can be attributed to the different amounts of alloying elements. As mentioned above, the Mo

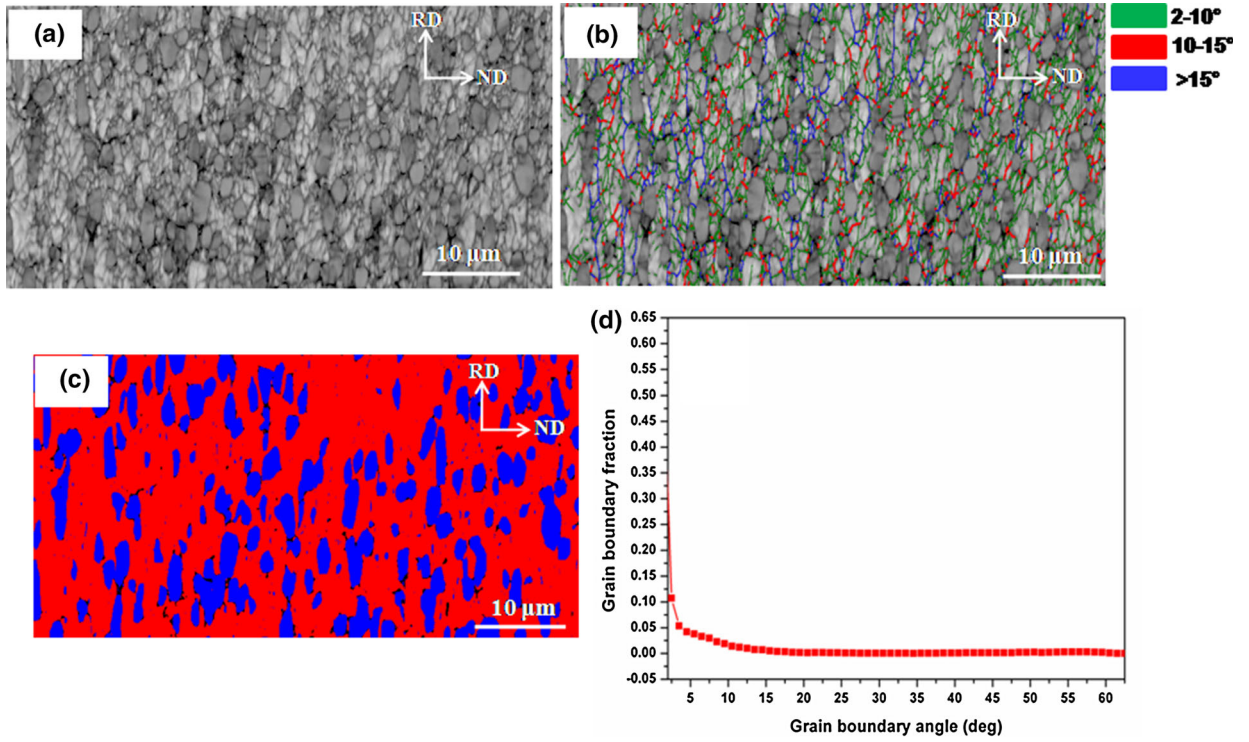


Fig. 15—Microstructures of the 70 pct hot-rolled alloy A2 (a) band contrast, (b) grain boundary map, (c) distribution of  $\alpha$ -phase (blue) in beta matrix (red), and (d) grain boundary distribution obtained by EBSD technique (Color figure online).

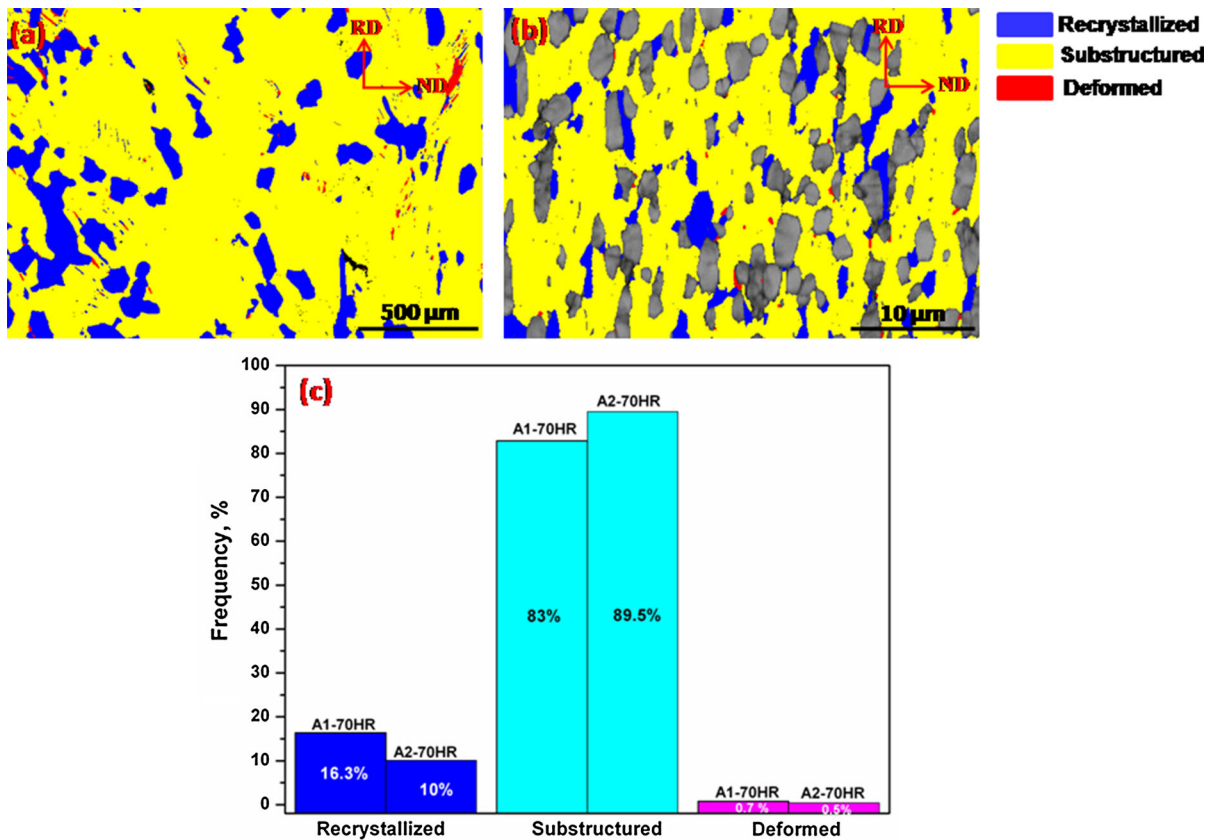


Fig. 16—Microstructure maps of the 70 pct hot-rolled alloys (a) A1, (b) A2, and (c) bar chart showing pct of recrystallized, substructured, and deformed microstructures obtained by EBSD technique (Color figure online).



equivalent has been kept same for the four alloys, but these alloys exhibit different  $\beta$  transus temperatures. In addition, diffusivity and partitioning of the alloying elements as well as the extent of solid solution are quite different.<sup>[24]</sup> It has been shown that the order of diffusivity and partitioning of the  $\beta$  stabilizing elements in present alloys are  $\text{Mo} < \text{Cr} < \text{V}$  and  $\text{Cr} > \text{Mo} > \text{V}$ , respectively. However, the relative contribution of these two effects is too intricate to determine due to uncertainties of the available experimental data.

## V. CONCLUSIONS

1. Alloying elements have marked influence on the evolution of microstructures and textures in alloys Ti-5Al-5Mo-5V-3Cr (A1), Ti-5Al-3.5Mo-7.2V-3Cr (A2), Ti-5Al-5Mo-8.6V-1.5Cr (A3), and Ti-5Al-3.5Mo-5V-3.94Cr (A4) during hot rolling.
2. The microstructures of alloys A1 and A3 show partially recovered large and small fraction of recrystallized grains. The alloy A2 displays subgrains and recrystallized grains, while the alloy A4 exhibits the microstructure consisting of the features of both the alloys A1 and A2.
3. Shear bands within the prior  $\beta$  grains have been observed in the alloys A1, A3, and A4 having small volume fraction of the  $\alpha$  phase.
4. Both the alloying elements and hot rolling reductions have marked influence on the evolution of microstructures and textures.
5. The dominance of deformation and/or recrystallization components in respective  $\alpha$  and  $\gamma$  fibers varies with alloy compositions and hot rolling reductions. In alloys A1 and A2, deformation components dominate from 30 to 50 pct rolling reductions, while recrystallization components govern in 70 pct rolled samples. The deformation components prevail from 30 to 70 pct rolling reductions in alloy A3. The alloy A4 exhibits softening of texture due to recovery or early stage of recrystallization from 30 to 50 pct reductions, while texture present in 70 pct rolled sample consists mainly of the deformation components.
6. The role of molybdenum (Mo) appears to be quite critical in the evolution of microstructures and textures of these alloys. The alloys with low and high Mo contents display high and low amount of the  $\alpha$  phase, respectively.

## ACKNOWLEDGMENTS

The authors wish to acknowledge Defence Research and Development Organization for financial support. We are grateful to Dr. Amol A Gokhale, Director, Defence Metallurgical Research Laboratory for his

kind encouragement. We also acknowledge titanium alloy and metal working groups for their kind help.

## REFERENCES

1. D. Qin, Y. Lu, Q. Liu, and L. Zhou: *Mater. Sci. Eng. A*, 2013, vol. A56, pp. 460–67.
2. D. Qin, Y. Lu, K. Zhang, Q. Liu, and L. Zhou: *Mater. Charact.*, 2012, vol. 73, pp. 77–80.
3. E.W. Collings: *Physical Metallurgy of Titanium Alloys*, ASM, Materials Park, OH, 1984.
4. D. Qin, Y. Lu, Q. Liu, L. Zheng, and L. Zhou: *Mater. Sci. Eng. A*, 2013, vol. A572, pp. 19–24.
5. J.C. Fanning and R.R. Boyer: in *Titanium 2003: Science and Technology*, G. Luetjering and J. Albrecht, eds., Wiley-VCH, Hamburg, Germany, 2003, vol. IV, pp. 2643–50.
6. J.D. Cotton, R.R. Boyer, and R.D. Briggs, R.G. Baggerly, C.A. Meyer, M.D. Carter, W. Wood, G. Tewksbury, V. Li, and X. Yao: *Titanium 2007: Science and Technology*, M. Niinomi, S. Akiyama, M. Hagiwara, M. Ikeda, and K. Maruyama, eds., The Japan Institute of Metals, Kyoto, Japan, 3–7 June, 2007, vol. I, pp. 471–74.
7. A. Settefrati, M. Dehmas, G. Geandier, B. Denand, E.A.-Gautier, B. Appolaire, G. Khelifati, and J. Delfosse: *Titanium 2011: Science and Technology*, L. Zhou, H. Chang, Y. Lu, and D. Xu, eds., Science Press, Beijing, 19–24 June 2011, vol. I, pp. 468–72.
8. R.R. Boyer and R.D. Briggs: *J. Mater. Eng. Perform.*, 2005, vol. 14, pp. 681–85.
9. R.R. Boyer: *J. Met.*, 1994, vol. 46, pp. 20–23.
10. A. Hasegawa, S. Ishigai, and T. Matsushita: *6th World Conf. on Titanium*, P. Lacombe, R. Tricot, and G. Beranger, eds., Les Editions de Physique, Les Ulis, Cannes, France, 1988, pp. 1263–68.
11. A. Ghosh, S. Sivaprasad, A. Bhattacharjee, and S.K. Kar: *Mater. Sci. Eng. A*, 2013, vol. A568, pp. 61–67.
12. J.C. Fanning, S.L. Nyakana, K.M. Patterson, and R.C. McDaniel: *Titanium 2007: Science and Technology*, M. Niinomi, S. Akiyama, M. Hagiwara, M. Ikeda, and K. Maruyama, eds., The Japan Institute of Metals, Kyoto, Japan, 3–7 June, 2007, vol. I, pp. 499–502.
13. V. Venkatesh, M. Kamal, and J. Fanning: *Titanium 2007: Science and Technology*, M. Niinomi, S. Akiyama, M. Hagiwara, M. Ikeda, and K. Maruyama, eds., The Japan Institute of Metals, Kyoto, Japan, 3–7 June, 2007, vol. I, pp. 503–06.
14. N.G. Jones, R.J. Dashwood, M. Jackson, and D. Dye: *Scripta Mater.*, 2009, vol. 60, pp. 571–73.
15. N.G. Jones, R.J. Dashwood, M. Jackson, and D. Dye: *Acta Mater.*, 2009, vol. 57, pp. 3830–39.
16. S. Nag, R. Banerjee, R. Srinivasan, J.Y. Hwang, M. Harper, and H.L. Fraser: *Acta Mater.*, 2009, vol. 57, pp. 2136–47.
17. P.J. Arrazola, A. Garay, L.M. Iriarte, M. Armendia, S. Marya, and F. Le Maitre: *J. Mater. Process. Technol.*, 2009, vol. 209, pp. 2223–30.
18. N.G. Jones, R.J. Dashwood, D. Dye, and M. Jackson: *Mater. Sci. Eng. A*, 2008, vol. A490, pp. 369–77.
19. A. Dehghan-Manshadi and R.J. Dippenaar: *Mater. Sci. Eng. A*, 2011, vol. A528, pp. 1833–39.
20. I. Weiss and S.L. Semiatin: *Mater. Sci. Eng. A*, 1998, vol. A243, pp. 46–65.
21. C. Li, X.-Y. Zhang, K.-C. Zhou, and C.-Q. Peng: *Mater. Sci. Eng. A*, 2012, vol. A558, pp. 668–74.
22. N.G. Jones, R.J. Dashwood, D. Dye, and M. Jackson: *Metall. Mater. Trans. A*, 2009, vol. 40A, pp. 1944–54.
23. N.G. Jones, R.J. Dashwood, D. Dye, and M. Jackson: *Titanium 2011: Science and Technology*, L. Zhou, H. Chang, Y. Lu, and D. Xu, eds., Science Press, Beijing, 19–24 June, 2011, vol. I, pp. 226–30.
24. C.F. Yolton, F.H. Froes, and R.F. Malone: *Metall. Trans. A*, 1979, vol. 10A, pp. 132–34.
25. M.R. Barnett: *ISIJ Int.*, 1998, vol. 38, pp. 78–85.
26. L.E. Murr and E.V. Esquivel: *J. Mater. Sci.*, 2004, vol. 39, pp. 1153–68.

27. Y. Yang, H.G. Zheng, Z.D. Zhao, Q. Zhang, Q.M. Zhang, F. Jiang, and X.M. Li: *Mater. Sci. Eng. A*, 2011, vol. A528, pp. 7506–13.
28. G. Qiang, W. Qing, S.D. Li, H. Xiu-Li, and W. Gao-Hui: *Mater. Sci. Eng. A*, 2010, vol. A527, pp. 4229–32.
29. F.J. Humphreys and M. Hatherly: *Recrystallization and Related Annealing Phenomena*, 2nd ed., Elsevier, Oxford, 2004.
30. P. Manda, U. Chakkingal, and A.K. Singh: *Mater. Charact.*, 2014, vol. 96, pp. 151–57.
31. D. Raabe and K. Lucke: *Mater. Sci. Forum*, 1994, vols. 157–162, pp. 597–610.
32. D. Raabe and K. Lucke: *Scripta Metall.*, 1992, vol. 27, pp. 1533–38.
33. A.K. Singh, A. Bhattacharjee, and A.K. Gogia: *Mater. Sci. Eng. A*, 1999, vol. A270, pp. 225–30.
34. N.P. Gurao, A.A. Ali, and S. Suwas: *Mater. Sci. Eng. A*, 2009, vol. A504, pp. 24–35.